Frequency-Domain Analysis of Atmospherically Forced versus Intrinsic Ocean Surface Kinetic Energy Variability in GFDL's CM2-O Model Hierarchy

AMANDA K. O'ROURKE AND BRIAN K. ARBIC

Earth and Environmental Sciences, University of Michigan, Ann Arbor, Michigan

STEPHEN M. GRIFFIES

NOAA Geophysical Fluid Dynamics Laboratory, and Princeton University, Princeton, New Jersey

(Manuscript received 13 January 2017, in final form 1 August 2017)

ABSTRACT

Low-frequency variability at the ocean surface can be excited both by atmospheric forcing, such as in exchanges of heat and momentum, and by the intrinsic nonlinear transfer of energy between mesoscale ocean eddies. Recent studies have shown that nonlinear eddy interactions can excite an energy transfer from high to low frequencies analogous to the transfer of energy from high to low wavenumbers (small to large spatial scales) in quasi-two-dimensional turbulence. As the spatial inverse cascade is driven by oceanic eddies, the process of energy exchange across frequencies may be sensitive to ocean model resolution. Here a cross-spectrum diagnostic is applied to the oceanic component in a hierarchy of fully coupled ocean–atmosphere models to address the transfer of ocean surface kinetic energy between high and low frequencies. The cross-spectral diagnostic allows for a comparison of the relative contributions of coupled atmospheric forcing through wind stress and the intrinsic advection to low-frequency ocean surface kinetic energy. Diagnostics of energy flux and transfer within the frequency domain are compared between three coupled models with ocean model horizontal resolutions of 1°, 1/4°, and 1/10° to address the importance of resolving eddies in the driving of energy to low frequencies in coupled models.

1. Introduction

Increasing complexity in coupled ocean–atmosphere models has led to an ever-improving understanding of the climate system. Higher-resolution ocean models, which permit or resolve mesoscale ocean eddies, agree more closely with satellite observations of surface kinetic energy than lower-resolution models do (Maltrud and McClean 2005; Delworth et al. 2012; Griffies et al. 2015). The inclusion of ocean eddy dynamics in climate models provides a better overall representation of the ocean circulation across space and time scales, including the long time scales associated with intrinsic variability and climate change. Accurate simulations of climate change are sensitive to the representation of eddies and mixing, particularly in regions such as the North Atlantic and the Southern Ocean where eddy mixing transfers surface signals into the deep circulation (Farneti et al. 2010; Griffies et al. 2015; von Storch et al. 2016). Eddies also play a role in low-frequency variability of the ocean surface, such as in the modulation of the Kuroshio Current Extension (Wang and Koblinsky 1995; Qiu and Chen 2005) and coupled air–sea interaction leading to Pacific decadal variability (Barnett et al. 1999).

We may then expect the representation and resolution of oceanic eddies to influence the energetics of the ocean surface at low frequencies in coupled climate models. Here we use the transfer diagnostic of Arbic et al. (2012, 2014) to quantify the relative contributions of wind stress and nonlinear advection to the budget of ocean surface kinetic energy across three coupled climate models with varying horizontal resolution in the ocean model component. This diagnostic, also known as the cross-spectrum diagnostic of Hayashi (1980) (see also Stull 2009), decomposes the source or sink of energy due to a given process as a function of spectral frequency or wavenumber. An extensive description of the cospectral diagnostic and its relationship to the transfer of kinetic energy in an atmospheric context is described in Saltzman (1957) and Hayashi (1980). A rigorous derivation of the transfer

Corresponding author: Amanda K. O'Rourke, orourkea@umich.edu

DOI: 10.1175/JCLI-D-17-0024.1

equation in the frequency domain can be found in Morten (2015).

The surface kinetic energy budget can be influenced by many terms, as discussed in the context of the idealized quasigeostrophic model used in Arbic et al. (2014). Arbic et al.'s (2014) analysis of observations and realistic ocean models was, however, limited to the contribution of nonlinear advection to the kinetic energy budget. Arbic et al. (2014) used the Hybrid Coordinate Ocean Model (HYCOM) run as a stand-alone ocean model (i.e., forced by an atmosphere but not coupled to it), and the Archiving, Validating, and Interpretation of Satellite Oceanographic data (AVISO) observational product to investigate the transfer of energy to long time scales due to the nonlinear advective term. Here we use three fully coupled climate models to determine the impact of wind stress as well as nonlinear advection on the oceanic kinetic energy budget.

We focus primarily on the transfer diagnostic in the frequency domain. As such, we can use the transfer diagnostic to compare the relative contributions of wind power input and nonlinear advective dynamics to low-frequency oceanic variability at mesoscale and lower frequencies. Additionally, the cross-spectrum transfer diagnostic in frequency can be applied to any model grid point such that we are able to map the geographic distribution of these two contributions to low-frequency variability. We focus on wind forcing and nonlinear oceanic advection because we are able to compute these terms from the available output and because they contribute significantly to low-frequency variability.

It should be noted that we use the term "low-frequency variability" to refer to energy contained at long (months and greater) time scales rather than to the diagnosis of specific dynamical modes of variability such as ENSO, the Pacific decadal oscillation, or the variability of the Atlantic meridional overturning circulation (AMOC). We execute our diagnostics in a suite of model runs performed at different horizontal resolutions in the ocean model, anticipating that both the advective and wind stress contributions to the energy budget will be sensitive to the representation of eddies. Additionally, transfers via nonlinear advection are a signature of processes associated with geostrophic eddies, which are better resolved as the ocean model horizontal resolution is refined.

The tendency of eddy–eddy interactions in quasi-two-dimensional flows to drive energy across spatial scales has been extensively studied as a part of the geostrophic turbulence literature (Charney 1971; Rhines 1979; Salmon 1980; Scott and Wang 2005). In the geostrophic inverse cascade, energy in a fluid confined to roughly two dimensions, such as that of the ocean surface due to the effects of rotation (Vallis 2006, section 8.3.1), is transferred from small spatial scales, such as in unorganized turbulence, up to larger structures like coherent eddies and jets. Previous work by Arbic et al. (2012, 2014) suggests that a similar exchange of energy can be observed in the frequency domain, wherein ocean surface kinetic energy is transferred out of high-frequency motions and into low-frequency motions. Given this exchange of energy, the inclusion of high-frequency mesoscale eddies within a coupled climate model may impact the kinetic energy budget at lower frequencies. Correspondingly, we hypothesize that models that better resolve ocean eddies have more energy at low frequencies associated with the nonlinear transfer of energy from high frequency to low frequency. Testing this hypothesis is a primary focus of this paper.

We use the NOAA Geophysical Fluid Dynamics Laboratory (GFDL) hierarchy of coupled climate models (Delworth et al. 2012; Griffies et al. 2015) to compute frequency-dependent energy budget terms and to determine the extent to which ocean model horizontal resolution impacts the surface kinetic energy budget at long time scales. We address three primary issues related to this topic following the work of Arbic et al. (2012, 2014).

First we examine whether, within these GFDL simulations, nonlinear advection within the ocean surface can drive energy exchanges between frequencies in an analogous manner to that of the inverse cascade in wavenumber space. Using a cospectral diagnostic, we determine whether surface geostrophic kinetic energy is transferred from high to low frequencies due to advection in three fully coupled climate models. This transfer diagnostic can identify a "temporal inverse cascade" as an extraction of energy at high frequencies (negative transfer) and a source of energy (positive transfer) at low frequencies. The advective transfer of energy within the ocean surface has been described previously by Arbic et al. (2012, 2014) using an idealized model, satellite altimeter observations, and stand-alone ocean general circulation models.

Second, we compare the frequency-domain spectral kinetic energy transfer, where the transfer is also known as the divergence of the spectral kinetic energy flux (Scott and Wang 2005; Arbic et al. 2012, 2014), due to nonlinear advection to that of the direct energy input by the wind stress acting on the ocean surface. The magnitude of the transfer at a given frequency will then illustrate the relative impact of the wind stress and advective terms on the kinetic energy budget. As these models are fully coupled, changes in the ocean eddy field will have an impact on the overlying wind stress field (Duhaut and Straub 2006). Furthermore, changes in the

atmospheric wind stress field can influence the ocean eddy state (Xu et al. 2016). Thus atmospheric forcing due to wind stress is not wholly uncoupled from the advective transfer of energy. It is therefore not strictly correct to think of the wind forcing as entirely "external" to the ocean, or of the oceanic advection as entirely "internal."

Last, we examine the impact of better model representation of eddies with increasing model resolution. Our primary focus is on the effect of model resolution on spectral energy transfers, but we will also quantify the effect of resolution on spectral energy levels. Penduff et al. (2010, 2011) showed that increasing horizontal resolution in ocean models results in a better agreement between modeled and observed interannual sea level anomalies. The results of Penduff et al. (2010, 2011) suggest a mechanism such as that of Arbic et al. (2012, 2014) linking the fast, small-scale eddy field with variability at low frequencies. Model hierarchies similar to that of GFDL CM2-O (to be defined in section 2) have been used in previous studies to address the impact of horizontal ocean circulation on large-scale climate simulations (Roberts et al. 2004; Kirtman et al. 2012; Small et al. 2014; Roberts et al. 2016), but none has yet considered the spectral properties of the kinetic energy transfer and its sensitivity to resolution.

We begin in section 2 with a description of the three fully coupled models that are included in the GFDL CM2-O model hierarchy. The transfer diagnostic is introduced in section 3, which also describes the relation of the transfer to the wind power input in physical space (by which we mean the nonspectral domain). We confirm that the transfer diagnostic supports the inverse cascade of energy in wavenumber space in section 4. The bulk of our analysis focuses on the transfer and flux of surface kinetic energy in frequency space due to advection and wind stress forcing. The frequency-domain transfer of kinetic energy is considered in section 5 for the globe and for three dynamically distinct regions. Maps of the flux, or the integral of the transfer over certain frequency bands, are described in section 6. Finally, we summarize the key points of this work and discuss its implications in section 7.

2. The GFDL CM2-O model hierarchy

We use the NOAA Geophysical Fluid Dynamics Laboratory's (GFDL) CM2-O hierarchy of fully coupled climate models. Full model details can be found in Delworth et al. (2012) and Griffies et al. (2015). The hierarchy consists of three models with varying nominal ocean model horizontal resolution: CM2–1d at 1°, CM2.5 at 0.25°, and CM2.6 at 0.10°. The ocean component of all three models has 50 vertical levels. CM2–1d includes a 0.33° equatorial waveguide and mesoscale eddy parameterization within the tracer budget following Dunne et al. (2012). CM2.5 and CM2.6 do not include a mesoscale eddy parameterization in their tracer equation, thus facilitating our ability to directly assess the importance of horizontal grid resolution on the energetics of low-frequency variability. A more detailed discussion of the choices of mesoscale eddy parameterization in the CM2-O model hierarchy can be found in Griffies et al. (2015).

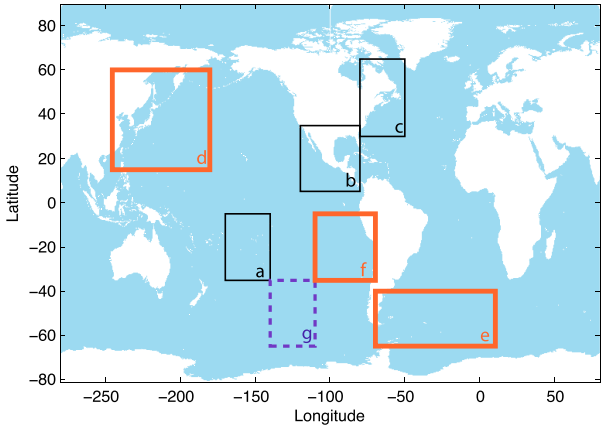

FIG. 1. Global ocean regions used for calculations. Regions A–C are regions in which recalculated wind stress is compared. Regions D–F are used for frequency analysis. Region G is an open ocean region with no land, in which frequency–wavenumber analysis is performed.

All three ocean models are coupled to an atmospheric model with 50-km horizontal resolution. Additionally, all three models have identical land and sea ice configurations (Delworth et al. 2012). The models are run under constant 1990 radiative forcing and have 140 years' worth of available output. We use 20 years of output from the available 140-yr runs for our analysis. All model atmospheric and oceanic fields are regridded to a regular latitude–longitude grid. The mixed layer depth is linearly interpolated to this grid to preserve its sign, while all other fields are regridded using a cubic spline.

Because of memory constraints on the calculations performed here, we show detailed results for only select regions as highlighted in Fig. 1. Global calculations are performed on open ocean regions, where open ocean is defined here as regions not within three grid points of land and not within a marginal sea, such as the Mediterranean Sea and Hudson Bay. We additionally exempt latitudes poleward of 65° due to analysis complexities associated with seasonal ice cover.

We require daily model output in order to capture variability at fast time scales. Because of the size of the CM2.6 simulation daily output is restricted to sea surface temperature (SST), sea surface height (SSH), and sea surface salinity (SSS) fields. As such, any calculations requiring velocity will be performed using geostrophic fields based on SSH output from all models. We find qualitatively and quantitatively similar results using either geostrophic or full (ageostrophic + geostrophic) velocities in CM2.5 such that we do not expect our use of geostrophic velocities to influence the overall conclusions of this work. The daily mixed layer depth in CM2.6 is calculated from a linear interpolation of the monthly mean mixed layer depth. The daily mixed layer depth is available in CM2.5 and CM2–1d and is used in computations made from these models.

Recalculation of daily wind stress

For all models, the wind stress is calculated from daily-averaged atmospheric fields using an iterative scheme based on the Monin–Obukhov similarity theory employed in the CM2-O model hierarchy itself. This offline calculation is performed due to a lack of saved daily stress in CM2.6. This scheme produces a wind stress that is dependent on the atmospheric stability as determined by the bulk Richardson number and the atmospheric and ocean surface velocities (Stull 2009).

As daily wind stress is saved in CM2.5 we can use this model as a benchmark to test the skill of our wind stress recalculation against the wind stress given in actual model output. Figure 2 shows a grid point by grid point comparison of the recalculated versus actual daily-averaged wind stress fields over years 15–20 in three distinct regions of CM2.5. We choose these three sample regions, displayed as regions A, B, and C in Fig. 1, based on their comparatively different land percentage and seasonal ice cover. There is strong agreement between model and recalculated zonal and meridional components of the wind stress, with correlation coefficients between the recalculated values and actual model output ranging from 0.984 to 0.997 for the three test regions. While the use of daily-averaged winds can lead to an underestimate in the wind stress (Zhai et al. 2012), we find that the agreement between our wind stress recalculation based on daily averaged winds and the daily averaged wind stress output from the model is sufficiently close for our analysis.

The open ocean region of the South Pacific (Fig. 2a) reveals the best agreement between the recalculation and model output with correlation coefficients of 0.997 and 0.993 for the zonal and meridional components of the wind stress, respectively. We find that the presence of land does not greatly inhibit our ability to accurately recalculate the wind stress. In the Gulf of Mexico (Fig. 2b) there is more spread between models and recalculations than in the open ocean region shown in Fig. 2a. Nonetheless, we are still able to accurately represent the daily wind stress using daily averaged atmospheric and oceanic fields.

The greatest inaccuracies occur in regions with seasonal ice cover, such as in the North Atlantic region shown in Fig. 2c. Here the spread between model and recalculated wind stress is large relative to that of Figs. 2a and 2b; correlation coefficients are 0.986 and 0.984 for zonal and meridional components of wind stress, respectively. The larger error spread is due to the presence of seasonal ice within part of this domain. For this reason we restrict our analysis to latitudes equatorward of 65°.

3. Energy transfer analysis

a. Kinetic energy equation

The budget equation for ocean surface kinetic energy following Gregory and Tailleux (2011), in units of $\mathrm{W\,m^{-2}}$, can be expressed as

$$(\rho_0 H)\frac{1}{2}\frac{\partial}{\partial t}(u^2+v^2) = -(\rho_0 H)\underbrace{[u(\mathbf{u}\cdot\nabla u)+v(\mathbf{u}\cdot\nabla v)]}_{\text{Horizontal Advection}} + \underbrace{[u\tau_x + v\tau_y]}_{\text{Wind Stress}} - \underbrace{H(\mathbf{u}\cdot\nabla_h p)}_{\text{Pressure Work Term}}$$
$$+ (\rho_0 H)\underbrace{\left[u\left(w\frac{\partial u}{\partial z}\right)+v\left(w\frac{\partial v}{\partial z}\right)\right]}_{\text{Vertical Advection}} + \underbrace{H\mathbf{u}\cdot\mathbf{F}_v}_{\text{Vertical Diffusion}} + \underbrace{H\mathbf{u}\cdot\mathbf{F}_h}_{\text{Horizontal Diffusion}} . \quad (1)$$

Here $\mathbf{u} = (u, v)$ are the horizontal velocity components in the x (zonal) and y (meridional) directions, w is the vertical velocity within the subsurface, τ_x and τ_y are the zonal and meridional surface wind stresses, $\rho_0 = 1027$ $\mathrm{kg\,m^{-3}}$ is the constant ocean reference density, p is the pressure, and H is the mixed layer depth. Vertical and horizontal diffusive forcing, $\mathbf{F}_v$ and $\mathbf{F}_h$ respectively, include additional diffusive and viscous processes. The vertical coordinate is given as z and the horizontal gradient as ∇_h.

As outlined earlier, we focus on the relative contributions of the geostrophic component of the horizontal

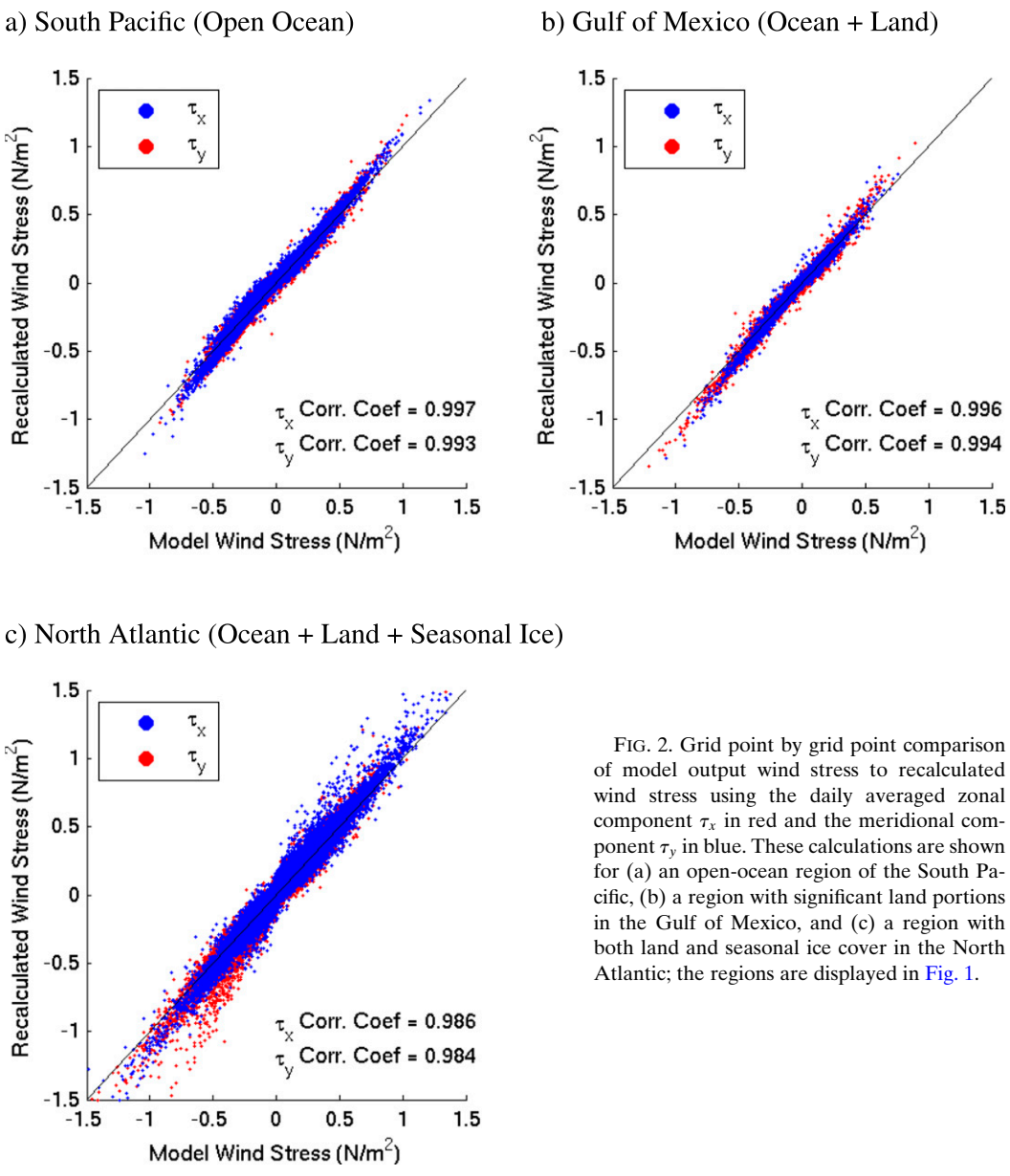

FIG. 2. Grid point by grid point comparison of model output wind stress to recalculated wind stress using the daily averaged zonal component τ_x in red and the meridional component τ_y in blue. These calculations are shown for (a) an open-ocean region of the South Pacific, (b) a region with significant land portions in the Gulf of Mexico, and (c) a region with both land and seasonal ice cover in the North Atlantic; the regions are displayed in Fig. 1.

advection and wind stress terms. That is, we perform a spectral transfer analysis using the geostrophic horizontal velocity field so that we approximate $\mathbf{u} \approx \mathbf{u}_g = (u_g, v_g)$. The geostrophic horizontal advection and wind stress terms of Eq. (1) may be written as

$$\begin{aligned}&\text{Geostrophic Horizontal Advection}\\&\quad = -(\rho_0 H)[u_g(\mathbf{u}_g \cdot \nabla u_g) + v_g(\mathbf{u}_g \cdot \nabla v_g)]\\&\text{Geostrophic Wind Stress}\\&\quad = u_g \tau_x + v_g \tau_y . \end{aligned} \tag{2}$$

The emphasis on geostrophic velocities in our analysis neglects additional ageostrophic components in the horizontal advection and wind stress terms. As such, the general formulation of the vertical advection, pressure work, and diffusion terms of (1) do not impact the conclusions presented herein. These terms are shown in (1) for completeness only and to emphasize that our analysis is unable to quantify the total energy budget and energy transfer within the ocean surface. Nonetheless, the inclusion of the wind stress term in the transfer analysis is more than was done in the analysis of realistic models by Arbic et al. (2012, 2014), who only considered the advective term.

We are interested in the energy input into the ocean surface. The pressure work term is then evaluated at $p = p_s$, where p_s is the surface pressure. The work done

by the atmospheric pressure on the ocean surface is not currently included in the GFDL CM2-O model suite. As such, it is neglected in this analysis.

b. Transfer equation

Arbic et al. (2012, 2014) used a diagnostic of the spectral transfer and flux of eddy kinetic energy at given frequencies and wavenumbers due to nonlinear advection for three distinct datasets: a high-resolution stand-alone ocean-only model, satellite observations, and a quasigeostrophic idealized model. Here we consider the transfer of energy due to the nonlinear advection term, as in the stand-alone ocean-only models of Arbic et al. (2012, 2014). In contrast to these earlier papers, we also compute the transfer due to wind stress. The transfer of kinetic energy due to horizontal advection and wind stress driving are, respectively, defined as

$$T_A(x,y,\omega) = -\rho_0 \Re[\widehat{(u_g H)}^* \widehat{(\mathbf{u}_g \cdot \nabla u_g)} + \widehat{(v_g H)}^* \widehat{(\mathbf{u}_g \cdot \nabla v_g)}],$$
$$T_W(x,y,\omega) = +\Re[\hat{u}_g^* \hat{\tau}_x + \hat{v}_g^* \hat{\tau}_y]. \quad (3)$$

Here hats indicate the spectral transform of a given variable or field in frequency ω space, $\Re$ indicates the real part of a complex quantity, and asterisks (*) indicate the complex conjugate. Before a spectral transform is taken in ω space, the time mean and trend are removed from a given field and the results are windowed in time. Derivatives are taken in grid space using finite difference methods consistent with those used in the model itself.

The transfers as calculated in (3) are in units of $\mathrm{W\,m^{-2}}$ instead of $\mathrm{nW\,kg^{-1}}$ as in Arbic et al. (2012, 2014). We use $\mathrm{W\,m^{-2}}$ to better facilitate comparisons to papers that discuss wind power input into the ocean surface such as Wunsch (1998). Conversion between the two units requires the use of the mixed layer depth H and a constant density ρ_0. These terms only arise when considering the wind stress term, which was not computed in Arbic et al. (2012, 2014). We additionally utilize the discrete Fourier transform to obtain transfer spectra, in terms of $\mathrm{W\,m^{-2}}$, rather than spectral density. Spectral density units would include a normalization factor due to the spacing of the frequency vector, which is equal to $d\omega = 0.02$ cycles per year here. For spectral transfers in wavenumber, the normalization factor would be equal to the spacing of the wavenumber vector dk, with $dk = 2.4 \times 10^{-3}$ rad $\mathrm{km^{-1}}$ in our analysis. See Stull (2009, section 8.6.1) for a discussion of the units of spectra versus spectral density.

The transfer Eqs. (3) are given as functions of horizontal grid space (x, y). They can also be represented in terms of isotropic horizontal wavenumber k as in Arbic et al. (2014). When we discuss transfers in terms of wavenumber and frequency space, that is, $T_A(k, \omega)$, as in section 4, hats should be taken as spectral transforms in both time and space.

As noted in Hayashi (1980), the frequency-domain transfer equation between two arbitrary variables a and b can be interpreted as the spectrum of the sample covariance averaged over time, t, given the relationship

$$\sum_{\min(\omega)}^{\max(\omega)} T_{a,b}(\omega) = \sum_{\min(\omega)}^{\max(\omega)} \Re[\hat{a}(\omega)\hat{b}^*(\omega)] = \overline{a(t)b(t)}^t, \quad (4)$$

where the overline indicates the temporal average and $a(t)$ and $b(t)$ are two arbitrary quantities in time with corresponding frequency spectra of $\hat{a}(\omega)$ and $\hat{b}(\omega)$, respectively. Here $\min(\omega)$ and $\max(\omega)$ are the minimum and maximum resolved frequency.

The form of Parseval's theorem given in Eq. (4) can also be thought of as the frequency-dependent contribution of eddy kinetic energy by a given process, such as either advection or wind stress in (3), to the time-mean general circulation (Saltzman 1957). For instance, a negative $T_A(x, y, \omega)$ from (3) indicates the extraction of energy from the general circulation due to advection at a given location (x, y) and, more importantly, at a given frequency ω. Regions with high overall kinetic energy, such as in western boundary currents and the Southern Ocean, may have transfers of either sign.

The cospectral transfer calculations in Hayashi (1980) were primarily applied to the spatial-wavenumber domain as opposed to the temporal-frequency domain that we focus on here; however, the spectral methodology is similar in either case (Hayashi 1980). Arbic et al. (2014) discussed the frequency, wavenumber, and frequency–wavenumber properties of the nonlinear advective transfer term. Additionally, Arbic et al. (2012, 2014) used an energy equation derived from the quasigeostrophic potential vorticity equation, whereas Hayashi (1980) used the momentum form of the geostrophic kinetic energy equation. The transfer calculation can additionally be applied to other budgets, including enstrophy and potential energy, as discussed in Steinberg et al. (1971). Additional studies utilizing the spectral transfer calculation include Salmon (1978, 1980), Hua and Haidvogel (1986), Larichev and Held (1995), and LaCasce (1996), all of which focused on spectral transfers in the wavenumber domain.

c. Deformation and Rhines scales

We utilize the cospectral transfer diagnostic of (3) to investigate kinetic energy transfers within the ocean surface. Primarily, we are interested in how advective

transfers, which yield an inverse cascade in wavenumber space, appear in the frequency domain. Scott and Wang (2005) found that the geostrophic inverse cascade can be identified through the wavenumber spectral energy flux. The transfer diagnostics given in (3) may be considered the divergence of the spectral flux. Scott and Wang (2005) note that geostrophic kinetic energy is extracted by advection near wavelengths corresponding to the deformation radius, L_d, and cascades up to larger scales. The inverse cascade thus shows up as a sink in the advective transfer (negative T) at wavenumbers near the deformation radius and a source (positive T) at lower wavenumbers (larger length scales). For our analysis, the deformation radius L_D is taken from Chelton et al. (1998). Scott and Wang (2005) found that the arrest wavelength k_R for the inverse cascade is determined by the Rhines scale L_R given by

$$L_R = \frac{1}{k_R} = \sqrt{2U_{\mathrm{RMS}}/\beta}, \tag{5}$$

where U_{RMS} is a root-mean-square velocity and β is the gradient of the Coriolis parameter.

As we will be considering exchanges of energy in the frequency domain, it is worthwhile to note characteristic time scales based on the deformation and Rhines length scales discussed in Scott and Wang (2005). We define an arrest frequency based on the Taylor hypothesis dispersion relation,

$$\omega = U_{\mathrm{RMS}} k \tag{6}$$

where the frequency ω of a turbulent eddy is related to its wavenumber k through an advective, root-mean-square velocity U_{RMS} (Taylor 1938; Thorpe 2007). The deformation and Rhines frequencies are then respectively

$$\omega_D = U_{\mathrm{RMS}} L_D^{-1} \quad \text{and} \quad \omega_R = U_{\mathrm{RMS}} L_R^{-1}. \tag{7}$$

The transfer diagnostic quantifies the extraction or supply of energy at a particular spatial and/or temporal scale due to the actions of wind stress or advection. It must still be noted, however, that the spectral analysis of kinetic energy transfer across the frequency domain using (3) cannot diagnose any particular physical mode of low-frequency variability, such as the AMOC, or the impact of eddy resolution on any particular known mode of variability.

d. Wind stress terms in physical space

We now provide an interpretation of the wind stress term in Eq. (3) in physical space using the relationship given in Eq. (4) to provide a physical understanding of the transfer diagnostic. The time-mean wind stress term can be described as the sum of the contributions from the stationary, time-invariant flow and from that of the time-varying flow:

$$\underbrace{\overline{u_g}\,\overline{\tau_x} + \overline{v_g}\,\overline{\tau_y}}_{\text{total}} = \underbrace{\overline{u_g}\,\overline{\tau_x} + \overline{v_g}\,\overline{\tau_y}}_{\text{mean}} + \underbrace{\overline{u_g'\tau_x'} + \overline{v_g'\tau_y'}}_{\text{anomaly}}, \tag{8}$$

where overbars denote the time mean and primes denote anomalies from the time mean. For our calculations the time mean is taken over 20 years. Note again that here u_g and v_g are the geostrophic zonal and meridional velocities, and not the full (geostrophic plus ageostrophic) surface currents. Our usage of the geostrophic velocities is consistent with the definition of wind power given in Wunsch (1998) using altimeter data. Von Storch et al. (2007) find that using geostrophic velocities to calculate the wind power input is a good approximation (within 10% error) to the overall wind-generated power input into the deep ocean.

To perform the spectral transfer calculations given in Eq. (3), we remove the time mean and trend from each variable before taking the spectral transform. As such, the transfer calculation of (3) allows us to analyze the time-anomaly term of (8) by individual frequency contributions. The sum of the frequency-dependent transfer of (3) is equal to the time anomalous term of (8).

Figure 3 displays the total, mean, and anomalous contributions to the global wind power input, following Eq. (8), for CM2.6. Globally integrated, the total wind power input for CM2.6 is 1.06 TW as compared to 0.88 TW calculated in Wunsch (1998) and 1.06 TW in von Storch et al. (2007). The largest contribution to the total wind power (Fig. 3a) input is overwhelmingly from the time-mean (Fig. 3b) wind stress with only a small contribution from the anomalous inputs (Fig. 3c). Global integrals of the mean and anomalous wind power input are 0.99 and 0.07 TW, respectively, and agree well with the 0.84 TW (mean) and 0.04 TW (anomalous) calculations of Wunsch (1998). Von Storch et al. (2007) find time-mean and anomalous contributions of 0.92 and 0.14 TW, respectively.

Following Eq. (4), the sum of the high- and low-frequency wind stress flux in CM2.6 (Figs. 10a,b) is equal to the total anomalous wind stress power input shown in Fig. 3c. Within the strongly eddying regions, the time-mean wind power input is a positive source of ocean surface kinetic energy and is approximately an order of magnitude larger than the negative anomalous wind power input shown in Fig. 3c. The effects of anomalous wind stress and anomalous current interactions, as seen in Fig. 3c, have high negative amplitudes concentrated in

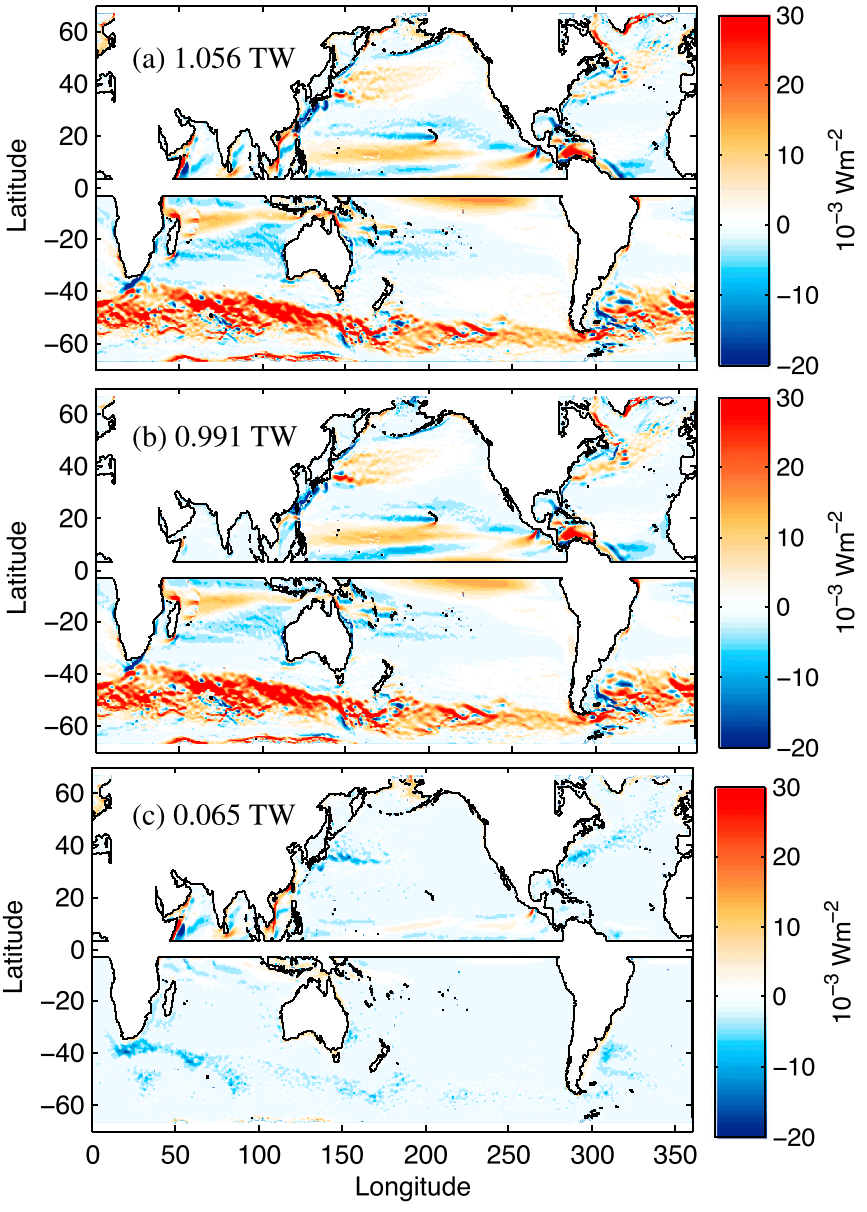

FIG. 3. Time-mean wind power input from (a) total, (b) mean, and (c) anomalous contributions in CM2.6. Units are in 10^{-3} W m^{-2}. Globally integrated wind power input for each contribution is given in units of TW.

the eddying regions of western boundary currents and the Southern Ocean.

Given that the bulk of the time-mean wind power input comes from the time-mean winds acting on the time-mean currents, as in Fig. 3b, we expect that ocean models with lower horizontal resolution may still reliably capture wind-driven modes of low-frequency variability in the absence of intrinsic eddy–eddy interaction. This expectation is consistent with the robustness of the Atlantic meridional overturning circulation (AMOC) seen in low-resolution models as discussed in Grégorio et al. (2015). Low-resolution models may therefore capture modes of wind-driven variability that are dynamically insensitive to the presence of eddies. Nonetheless, the presence of eddies may modify those modes on long time scales.

The calculation of spectral transfers, as in Eq. (3), allows us to further separate the time anomaly term of the wind stress, as in Eq. (8), and the action of the geostrophic advective term into contributions from individual frequencies following Eq. (4). We are then able to determine how low-frequency and high-frequency

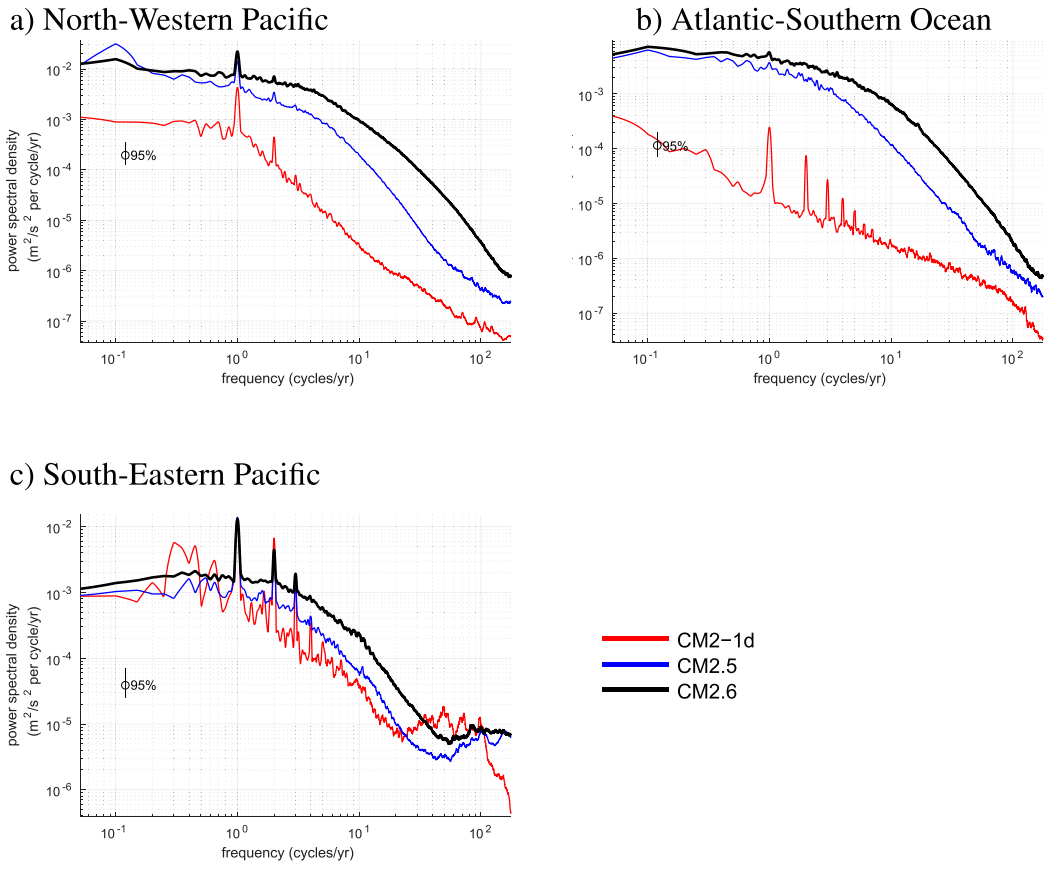

FIG. 4. Frequency spectral density of surface geostrophic kinetic energy for the (a) northwestern Pacific (region D), (b) South Atlantic–Southern Ocean (region E), and (c) southeastern Pacific (region F) in the CM2–1d (red), CM2.5 (blue), and CM2.6 (black) models (see Fig. 1 for regions). Spectra are averaged over all oceanic grid points within each subregion and a 15-point running mean is applied in frequency.

motion separately influence the time-mean anomalous energy input into the ocean through both the advective and wind stress transfer terms.

e. Surface kinetic energy spectra

Each of the three models within the CM2-O model hierarchy has varying ocean model horizontal resolution and thus varying total surface ocean energy. The total surface ocean kinetic energy can be thought of as the reservoir from which energy is extracted or supplied. For instance, the highest-resolution model, CM2.6, has sufficient horizontal resolution to support a vibrant eddy field with energy spread across temporal scales, as shown in the surface geostrophic kinetic energy spectra for three regions in Fig. 4.

Across strongly eddying midlatitude regions, including the northwestern Pacific (Fig. 4a) and the Atlantic sector of the Southern Ocean (Fig. 4b), the highest-resolution models are most energetic across all frequencies, particularly in the synoptic to yearly time scales. In these eddying regions, CM2.5 and CM2.6 have approximately the same energy in the lowest-frequency modes of one year and longer. This behavior suggests that the 1/4° model is as energetic as the 1/10° model at long time scales. The 1° model has energy at long time scales approximately two orders of magnitude less than that of the higher-resolution models, suggesting that the absence of eddies in low-resolution models may reduce the overall kinetic energy at long time scales.

Penduff et al. (2010, 2011) found that low-resolution ocean models had deficient sea surface height variability even at interannual time scales relative to observations. The kinetic energy spectra of Figs. 4a and 4b and the work of Penduff et al. (2010, 2011) indicate that sea surface variability at time scales longer than a year is sensitive to the representation of small-scale features of the ocean circulation, particularly in strongly eddying regions. Low-resolution ocean models (i.e., those with horizontal resolutions coarser than 1/4°; Penduff et al. 2010) may thus be unable to capture the ocean's intrinsic, eddy-driven variability on interannual time scales. These low-resolution models may, however, still

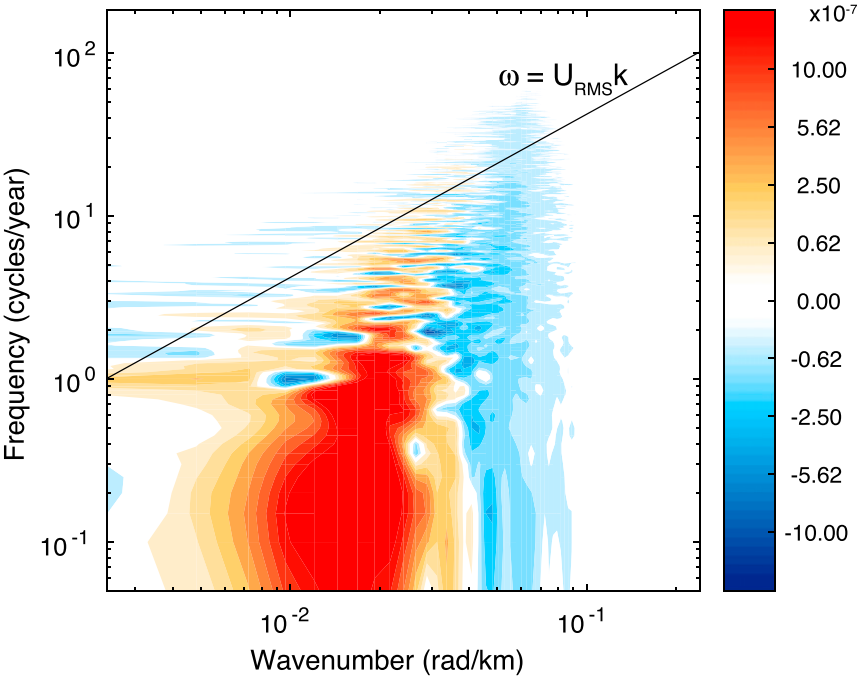

FIG. 5. Time-averaged advective transfer of kinetic energy in the South Pacific–Southern Ocean region of CM2.6 (see region G in Fig. 1) in units of $\mathrm{W\,m^{-2}}$, as a function of wavenumber in radians per kilometer and frequency in cycles per year. Transfers are Gaussian smoothed such that variations in the raw data are within $\pm 3.95 \times 10^{-8}\ \mathrm{W\,m^{-2}}$. The black line indicates the linear Taylor relation $\omega = U_{\mathrm{RMS}}k$, where $U_{\mathrm{RMS}} = 0.083\ \mathrm{m\,s^{-1}}$.

be able to capture large-scale, wind-driven modes of low-frequency variability.

While the kinetic energy frequency spectrum in strongly eddying midlatitude regions is dependent on ocean model horizontal resolution, in the tropical–subtropical weakly eddying region of the southeastern Pacific (Fig. 4c) the spectra display much less sensitivity to model resolution. Nonetheless, the surface kinetic energy of CM2.6 is still greater than that of the lower-resolution models over most frequencies. An interesting feature of the southeastern Pacific in Fig. 4c is the apparent buildup of energy at high frequencies within all three models. As this region is tropical, we suspect that this is a feature of fast linear waves near the equator. The kinetic energy spectra of other tropical regions (not shown) also display this behavior at short time scales.

4. Transfer in wavenumber–frequency space

Before considering transfers in frequency space, we examine an example of transfers in wavenumber–frequency space. Wavenumber-domain transfers are more familiar given the literature on the inverse cascade in quasi-two-dimensional turbulence (Salmon 1980; Vallis 2006; Scott and Wang 2005). Spectral transforms of any ocean field from space to an isotropic horizontal wavenumber require a relatively square region of open, island-free ocean. We can consider, for example, one strongly eddying, open-ocean region in the South Pacific and Southern Ocean, identified as region G in Fig. 1. Regions D–F in Fig. 1 contain horizontal discontinuities in the form of islands and coastlines that prohibit wavenumber analysis and will instead be the focus of frequency analysis in section 5. The South Pacific–Southern Ocean region is additionally a subdomain of that considered by Scott and Wang (2005). In this region we will relate characteristic length and time scales, such as those arising from the deformation radius and Rhines scales, to the frequency transfers of Eq. (3).

Advective transfers within the South Pacific–Southern Ocean region are shown in Fig. 5. The $k-\omega$ transfer has been Gaussian smoothed such that the raw transfer varies about the smoothed curve with a standard deviation of $3.95 \times 10^{-8}\ \mathrm{W\,m^{-2}}$. At high frequencies, there appears to be a linear relationship in the energy transfer between wavenumber and frequency, suggesting that high-frequency dynamics may follow the Taylor dispersion given in Eq. (6). Included in Fig. 5 is a Taylor dispersion curve for the computed root-mean-square velocity over the South Pacific–Southern Ocean box of $U_{\mathrm{RMS}} = 0.083\ \mathrm{m\,s^{-1}}$. The dispersion curve follows some of the transfers roughly, but not precisely.

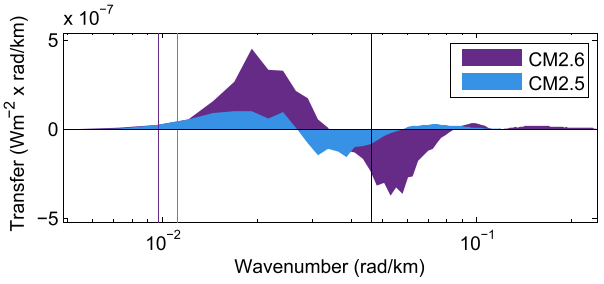

FIG. 6. Time-mean advective transfer of kinetic energy in the South Pacific–Southern Ocean region (region G in Fig. 1) as a function of wavenumber in radians per kilometer. Transfers in units of W m^{-2} are multiplied by the wavenumber vector in order to be area preserving on a logarithmic scale (Emery and Thomson 2014, section 5.4.3.4). The local deformation radius, based on the average latitude of the box, is given by a solid black line. Solid blue and purple lines indicate the area-averaged Rhines scales in CM2.5 and CM2.6, respectively.

Arbic et al. (2014) found that the wavenumber–frequency eddy kinetic energy (EKE) spectrum of the Agulhas region in HYCOM and AVISO did not strictly follow the Taylor dispersion relation, suggesting that more complex dynamics beyond passive advection by a root-mean-square velocity are at play within this region. Here we are considering the advective transfer, not the EKE spectrum, in wavenumber–frequency space. The transfer diagnostic represents a rate of change of the EKE as a function of (k, ω), and therefore we cannot expect a direct correlation between features in the EKE $k-\omega$ spectrum, including that of a dispersion relation, to apply to the advective transfer $k-\omega$ spectrum.

The pattern of transfer in frequency and wavenumber space in CM2.6 agree well with similar calculations of $T_A(k, \omega)$ in the ocean-only model and observational products discussed in Fig. 12 of Arbic et al. (2014). The kinetic energy transfer is more strongly dependent on wavenumber than on frequency. This dependence on wavenumber can be better illustrated by integrating $T_A(k, \omega)$ over all frequencies to obtain the transfer in wavenumber only, $T_A(k)$.

Nonlinear advective transfers in wavenumber space, $T_A(k)$, calculated using Eq. (3), follow the well-documented inverse cascade of energy as shown in Fig. 6 for the South Pacific–Southern Ocean in both CM2.5 and CM2.6. Transfers in Fig. 6, and in later plots of the frequency transfer, are multiplied by wavenumber (frequency) such that they are area preserving when displayed on a logarithmic scale (Emery and Thomson 2014, section 5.4.3.4; Stull 2009, section 8.6.4). Without multiplication by the wavenumber (frequency) vector, the sign of the high wavenumber (frequency) transfers would not be identifiable due to the nature of a logarithmic axis. The area under the transfer function represents the flux of energy into or out of certain frequencies. It is therefore useful to represent the transfers in an area-preserving manner. In addition, the transfers of Fig. 6 and later figures of the transfer calculation as a function of frequency are Gaussian smoothed in wavenumber and frequency, respectively. We do not show CM2–1d in Fig. 6 as the advective transfer is negligible due to a lack of eddy resolution.

In an inverse cascade, energy is extracted at small spatial scales determined by the local Rossby deformation radius L_D and supplied up to larger scales determined by the local Rhines scale as given in Eq. (5) (Scott and Wang 2005). Within the South Pacific–Southern Ocean region, energy is extracted $[T_A(k) < 0]$, in both CM2.5 and CM2.6, from scales near the wavelength $2\pi L_D = 138$ km. This extraction scale is similar to that found in Scott and Wang (2005).

Energy is supplied to wavelengths much larger than the deformation radius within both CM2.5 and CM2.6 as can be seen in the positive lobes of $T_A(k)$ at low wavenumbers in Fig. 6. The maximum positive energy transfer at large scales is centered around a wavelength of approximately 280 km. Positive energy transfers extend out to longer scales and appear to arrest near the Rhines wavelengths of $2\pi L_R = 565$ km and 641 km for CM2.5 and CM2.6, respectively. This behavior agrees well with the results of Scott and Wang (2005) in which the inverse cascade is halted at approximately the wavelength determined by the Rhines scale. The Rhines wavelengths for CM2.5 and CM2.6 differ slightly due to changes in U_{RMS} between the two models with $U_{\mathrm{RMS}} = 6.43$ and 8.35 cm s^{-1} in CM2.5 and CM2.6, respectively.

5. Advective and wind stress transfers in frequency space

a. *Advective transfer*

We consider the transfer of surface kinetic energy as a function of frequency for the three models in GFDL's CM2-O model hierarchy. The transfer of kinetic energy due to the advective and wind stress terms is shown in Fig. 7, as averaged over the global ocean, two strongly eddying regions (regions D and E in Fig. 1), and a relatively quiescent region (region F in Fig. 1).

In CM2–1d, the lowest-resolution model, advection plays a very small role in the overall kinetic energy balance due primarily to the lack of resolved mesoscale eddies. For CM2.6 and CM2.5, however, we find that the advective term in the kinetic energy budget tends to be negative at high frequencies and positive at low frequencies with overall amplitudes increasing with ocean model resolution. The sign of the kinetic energy transfer

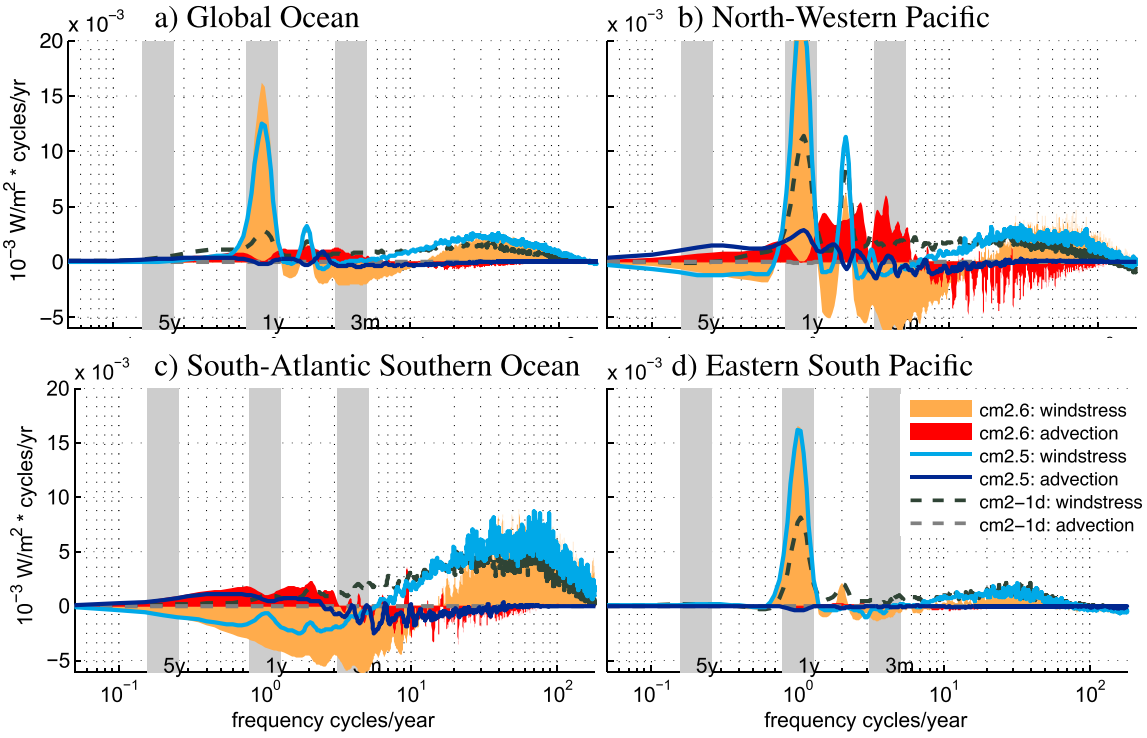

FIG. 7. Area-weighted transfers of geostrophic surface kinetic energy, multiplied by frequency and averaged over the (a) global ocean, (b) northwestern Pacific (region D in Fig. 1), (c) South Atlantic–Southern Ocean (region E in Fig. 1), and (d) southeastern Pacific (region F in Fig. 1) domains, for advection and wind stress as given in Eq. (3). Transfers are smoothed with a 15-point Gaussian window. Gray bands indicate periods of 5 years, 1 year, and 3 months.

term as a function of frequency in Fig. 7 indicates that internal interaction of ocean eddies leads to a removal of kinetic energy at high frequencies (negative transfer) and a source at low frequencies (positive transfer) within the eddying regions of the northwestern Pacific and South Atlantic–Southern Ocean (Figs. 7b and 7c). This result—that energy is transferred from high frequency to low frequency in eddying regions—is consistent with previous work by Arbic et al. (2012, 2014). It corresponds to an advective transfer toward longer time scales alongside the well-known inverse cascade in wavenumber space.

b. *Wind stress transfer*

The contribution to the time-mean kinetic energy budget from the wind stress is of an overall larger magnitude than that of the advective term at nearly all frequencies. All three ocean models are run under the same atmospheric model such that the differences in the wind stress transfer in Fig. 7 are primarily due to differences in ocean surface current velocities as given in Eq. (3). While changes in the ocean underlying the atmosphere may have impacts on both atmosphere and ocean circulation in a fully coupled model, we find that the spectra of the wind stress across the three models are comparable at all frequencies (not shown).

While the advective transfer term in CM2–1d is negligible, the wind stress transfer is of similar magnitude to the wind stress transfers of the higher-resolution models at periods less than 3 months (high frequencies). With the exception of the seasonal cycle and its 6-month harmonic, the high-resolution models of CM2.5 and CM2.6 have negative wind stress transfer at low frequencies. This negative transfer is particularly apparent in the eddying regions of Figs. 7b and 7c. At periods of approximately one year and a harmonic at 6 months, higher-resolution models appear to have a stronger kinetic energy transfer due to wind stress than that of CM2–1d, potentially due to a coupled eddy response that would be absent in noneddying models. The broadness of this seasonal peak in the wind stress calculation may be attributed to a 15-point Gaussian window smoothing applied to the transfers.

The similarity in the wind stress transfer calculation across all models, particularly at high frequencies, may suggest that these models share the same large-scale barotropic response to atmospheric forcing (Hirose et al.

2001). Hirose et al. (2001) note that the barotropic response of the ocean to wind stress forcing occurs at high frequencies and large spatial scales. In particular, the large-scale wind response occurs at periods of around 20 days consistent with the high-frequency range of enhanced wind stress transfer in Fig. 7. As this response is spatially broad, low-resolution models such as CM2-1d will have a similar wind stress response to models with higher horizontal resolutions. Additionally, the wind stress source of energy at high frequencies is likely at large spatial scales, unlike the extraction of energy due to advection, which is presumably associated with the action of small-scale eddies.

While wind stress is known to transfer energy into the ocean surface through near-inertial motions, the similarity of the wind stress transfer term at high frequencies across the three models is not likely due to these fast, small-scale features. The characteristic time scales of the positive wind stress transfer in Fig. 7 are at periods of 5 days to upwards of 3 months, consistent with the barotropic response, and are at much longer time scales than that of near-inertial motions, which are on the order of a few days throughout most of the midlatitudes (Jayne and Tokmakian 1997). Furthermore, we are using daily averaged fields for our analysis, which will filter out many very high-frequency signals such as that from near-inertial waves.

We can not a priori expect wind stress transfers to correlate with the geostrophic inverse cascade, as we might expect of the advection transfer. The geostrophic inverse cascade applies to nonlinear interactions of the ocean surface velocity field with itself (Vallis 2006). The wind stress term in the kinetic energy budget $\mathbf{u}_g \cdot \boldsymbol{\tau}$ of Eq. (1) is roughly linear, although there is some nonlinearity due to the dependence of the horizontal wind stress vector $\boldsymbol{\tau}$ on the horizontal geostrophic velocities $\mathbf{u}_g$ (Stull 2009). We thus do not expect to see an inverse cascade in frequency space for the wind stress term.

Indeed, we find that the wind stress term appears to oppose the advective term. In general, particularly in strongly eddying regions such as the South Atlantic Southern Ocean of Fig. 7c, the wind stress in CM2.6 and CM2.5 adds energy at high frequencies and removes energy from low frequencies with notable exceptions at the seasonal cycle and its 6-month harmonic. The greatest source of globally averaged wind-driven kinetic energy transfer across all three models is at the yearly time scale with a secondary peak at periods of 6 months (Fig. 7a). Within the South Atlantic Southern Ocean region (Fig. 7c), however, the yearly wind stress transfer peak is absent likely due to a lack of strong seasonality within the Southern Ocean relative to that of the Northern Hemisphere (Hoskins and Hodges 2005).

Zhai et al. (2012) noted that wind power input into the ocean surface is a strong function of the sampling frequency in model data. High-frequency wind stress forcing based on 6-hourly winds adds up to a 70% increase in wind power input relative to monthly measured winds, suggesting that high-frequency wind forcing is a significant and positive contribution to the kinetic energy budget—in agreement with the positive wind stress transfer we see at high frequencies. Zhai et al. (2012) additionally note a potential feedback mechanism, due to the difference in ocean surface eddy velocities and the wind velocity, that can systematically dampen ocean eddies (consistent with the results shown in Fig. 3), thus providing a physical mechanism for wind stress damping (a negative transfer) of the ocean surface kinetic energy budget. Verifying the pathways of energy exchange would require a complete energy budget, encompassing all of the terms in Eq. (1) in both physical and spectral space, in order to confirm the energy cycle and the relationship between the sign of the advective transfer and that of the wind stress transfer. The analysis of the precise physical mechanisms behind the structure of the advective and wind stress transfers is more feasible in an idealized model, such as the coupled quasi-geostrophic model of Hogg et al. (2003), and is beyond the scope of the three primary questions of this paper as described in the introduction.

c. *The period of transition between transfer sources and sinks*

In the higher-resolution models of CM2.6 and CM2.5, we see in Fig. 7 a similar characteristic frequency at which the transfer function transitions from source $[T(\omega) > 0]$ to sink $[T(\omega) < 0]$ in both the advection and wind stress terms, with notable exceptions for the transitions associated with the seasonal cycle. In both CM2.5 and CM2.6 the transition period between sources and sinks of kinetic energy due to the wind stress transfer term, which will be referred to herein as the transition period, appears, in general, to be at slightly higher frequencies than that of the advective term. The advective transfer transition period is at approximately 6 months in CM2.5 and 3 months in CM2.6 whereas the crossover time for the wind stress transfer term is at periods of approximately 1.5 months in CM2.5 and one month in CM2.6 as can be seen in the plots made from eddying regions (Figs. 7b,c).

The period of transition from an energy sink at high frequency to an energy source at low frequency in the advective term is shifted to lower frequencies in CM2.5 relative to CM2.6, particularly in the eddying regions shown in Figs. 7b and 7c. In the global average (Fig. 7a),

the transition periods of the advective and wind stress terms in CM2.6 are approximately 37 and 30 days, respectively. The transition period of CM2.5 is not as distinct as that of CM2.6 as shown in the globally averaged advective transfer of CM2.5 in Fig. 7a. However, the first major zero crossing of the globally averaged transfer term occurs at approximately 115 days. The wind stress transfer of CM2.5 transitions from a positive to negative transfer at approximately 36 days.

Within strongly eddying regions of the northwestern Pacific (Fig. 7b) and the South Atlantic Southern Ocean (Fig. 7c), the transition periods for both CM2.5 and CM2.6 are at similar time scales to that of the global average (Fig. 7a). The lowest-resolution model, CM2-1d, does not have a definitive transition period for either wind stress or advection.

The zonally averaged transfer of kinetic energy due to advection and wind stress within CM2.6 and CM2.5 as a function of latitude can be seen in Fig. 8. The patterns of advection and wind stress transfer as a function of latitude are largely consistent between CM2.5 and CM2.6 with the amplitude of the signal being the largest difference between the two models. Characteristic time scales based on the zonally averaged deformation radius and Rhines scale given in Eq. (7) are included.

Overall, the transfers of kinetic energy due to wind stress and advection have a weak dependence on latitude, but the tropics and midlatitudes display distinct characteristics. The midlatitudes, or latitudes poleward of approximately 30°, are characterized by advective transfer patterns we have already seen in the eddying regions of Figs. 7b and 7c. The advective term transfers energy out of high frequencies near the deformation time scale given in Eq. (7) and into all lower frequencies (Fig. 8a) corresponding to periods longer than the local Rhines time scale. The Rhines time scale, identified as a dashed curve in Fig. 8, approximately delineates the transition period at all latitudes. Unlike the transfer in wavenumber (Fig. 6), it appears that the Rhines frequency scale agrees more closely with the transition frequency between advective transfer source and sink rather than the arrest of the inverse cascade.

Within the midlatitudes there is positive advective transfer out to the lowest resolved frequencies corresponding to the 20-yr period of our analysis. Despite tapering to zero at low frequencies due to the multiplication of the transfer by the frequency vector, there is no distinct low frequency at which the advective term maximizes transfer in the midlatitudes, and thus no clear arrest time scale for the inverse cascade. This apparent tapering is a consequence of our desire for the transfers to be area-preserving on the logarithmic scale. If we had not multiplied by frequency in order to display area-preserving curves, the transfers would indeed be seen to be nonzero at long timescales, including beyond the 20-yr time scale we have considered here.

The midlatitudes display a two-mode structure in the advective transfer. Energy is extracted from high frequencies and added to low frequencies, with only one transition period centered approximately at a period of three months as seen in both the CM2.6 and CM2.5 results of Figs. 8a and 8c. Within the subtropics, however, there is a three-mode structure to the advective transfer. The advective transfer for periods longer than four months and shorter than one month is negative. Advection appears to pump kinetic energy out of motion at both high and low frequencies and into time scales of approximately three months within the subtropics, in ontrast to the behaviors seen in the midlatitudes.

The subtropics are likewise the location at which there is no clear separation between the deformation and Rhines time scales of (7), suggesting the underlying theory corresponding to the spatial inverse cascade may not apply equatorward of approximately 20°. Scott and Wang (2005) also find that the wavelength associated with an energy source no longer agrees well with that of the deformation radius equatorward of 30° and may be related to changes in the type of nonlinear instability present within the subtropics, notably in a shift away from midlatitude baroclinic instability and towards subtropical barotropic instability.

The CM2.6 and CM2.5 wind stress frequency transfer fields as a function of latitude (Figs. 8b and 8d) display more coherent features than are seen in the advective transfers. As we have seen in regional averages across all models in Fig. 7, the sign of the zonally averaged wind stress transfers in CM2.6 opposes that of the advective transfer term. Over much of the midlatitudes, energy is extracted across low frequencies and supplied to high frequencies by the wind stress term. Outside of the strongly eddying regions in the midlatitudes of either hemisphere, the trimodal structure found in the advective term again appears in the wind stress transfer term. Wind stress transfers in the subtropics extract energy from intermediate frequencies ranging from one to four months while adding kinetic energy to both higher and lower frequencies. Near the equator, wind stress transfers energy out of the highest frequencies. At latitudes poleward of approximately 40°N and 60°S wind stress appears to add energy at all frequencies.

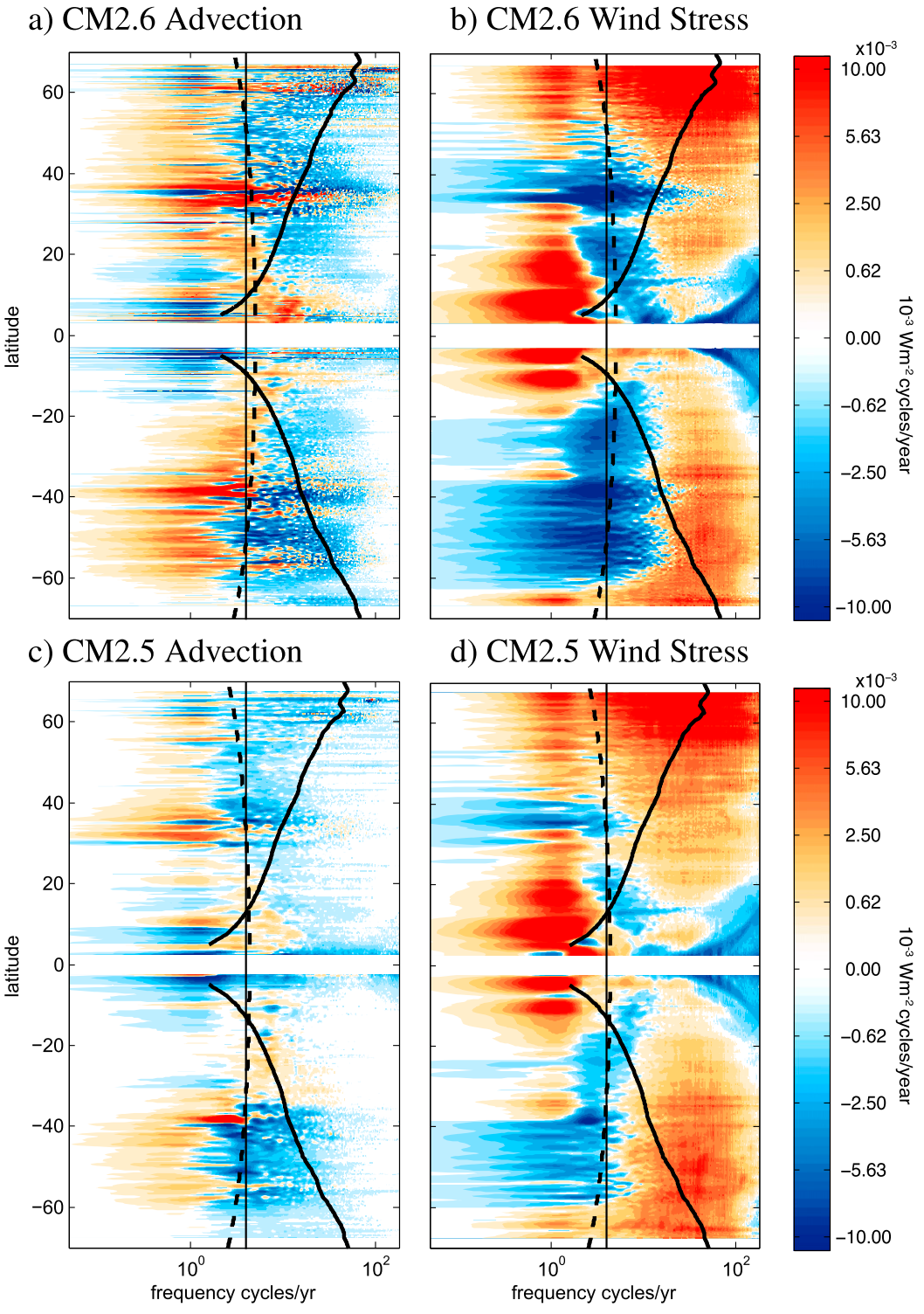

FIG. 8. Zonally averaged kinetic energy transfer as a function of latitude and frequency in 10^{-3} W m^{-2} cycles per year due to advection and wind stress in CM2.6 and CM2.5, respectively. The thin vertical black line represents a period of 3 months. Transfers have been multiplied by the frequency vector. Characteristic time scales associated with the deformation radius and Rhines scale are given in solid and dashed curves, respectively.

6. Flux of kinetic energy over low and high frequencies

Spectral flux is defined as the integral over the spectral transfers (Arbic et al. 2012, 2014; Scott and Wang 2005). Here we define the flux for a given term X as the sum of the transfers over a frequency bin (low or high) by

$$F_{X,\text{high}}(x,y) = \sum_{\omega_t}^{\max(\omega)} T_X(\omega,x,y),$$
$$F_{X,\text{low}}(x,y) = \sum_{\min(\omega)}^{\omega_t} T_X(\omega,x,y), \quad (9)$$

where ω_t is a chosen transition frequency and max(ω) [min(ω)] refers to the maximum (minimum) resolved frequencies. Based on the approximate 3-month period at which the midlatitude advective transfer term transitions from a negative transfer to a positive transfer in frequency space, we choose $\omega_t = 2\pi(3\,\text{months})^{-1}$ as the transition frequency. Three months is approximately the frequency associated with the Rhines scale as seen in Fig. 8. High- and low-frequency bins are then considered for frequencies higher and lower than the transition frequency, respectively.

Maps of the advective and wind stress fluxes over high- and low-frequency bins are shown in Figs. 9 and 10, respectively. Each of the three models is shown for comparison. The maps of geostrophic kinetic energy flux are based on grid point by grid point analysis and are thus inherently noisy. Spatially integrated transfer quantities over local regions, which show the Gaussian smoothed net behavior of $T_A(\omega)$ and $T_W(\omega)$ as a function of latitude (Fig. 8) and basin (Fig. 7), have been discussed in previous sections. Additionally, the globally integrated fluxes over both high and low frequencies [Eq. (9)] for all three models are given in Table 1.

The advective flux in Fig. 9 reveals a substantial spatial dependence on the location of eddies within the models, as well as patterns of positive and negative fluxes that are dependent on the presence of eddies. The advective fluxes of the two highest-resolution models, CM2.6 and CM2.5, generally agree in sign across high and low frequencies. There is more spatial variance in CM2.6 than in CM2.5 due to its more energetic eddy field. However, when spatially averaged, the transfers and fluxes within the Southern Ocean are comparable, as seen in Fig. 7c.

In most of the world's oceans, CM2.6 reveals stronger fluxes than CM2.5, likely due to the stronger eddy activity in CM2.6. In the global average, for instance, the high-frequency flux in CM2.6 is -7.35×10^{-3} TW as compared to that of -5.63×10^{-3} TW in CM2.5 (Table 1). The globally integrated flux at low frequencies is positive for both higher-resolution models at 6.51×10^{-3} and 24.30×10^{-3} TW in CM2.5 and CM2.6, respectively. The advective flux in CM2–1d is several orders of magnitude smaller than that of CM2.5 and CM2.6 and is only evident near the equator at low frequencies.

Despite large spatial variation in the sign of the advective flux shown in Fig. 9, the globally integrated high- and low-frequency advective transfers (Table 1) are net negative and positive, respectively. This behavior is consistent with the regional patterns seen in the advective transfers of Fig. 7, particularly in the eddying regions of the northwestern Pacific and the South Atlantic–Southern Ocean region (Figs. 7b,c). On average, the advective transfers in the eddying models of CM2.5 and CM2.6 act to remove energy at high frequencies and provide energy to low frequencies.

The surface geostrophic kinetic energy flux due to wind stress driving is shown in Fig. 10 and reveals a more basinwide signal relative to that of the advective flux, which is more strongly confined to that of eddying current systems. The wind stress flux is of comparable magnitude in CM2–1d and the higher-resolution models. At high frequencies there is a clear difference between negative tropical wind stress fluxes and positive wind stress fluxes within the midlatitude storm tracks across all models. At high frequencies there is a strong negative wind stress flux in regions of high eddy activity, such as the Southern Ocean and Kuroshio Current, that is more noticeable at higher horizontal resolutions. Although not specific to high frequencies, the damping of oceanic eddies by wind stress has been noted as a physical process by others, including von Storch et al. (2007), Zhai et al. (2012), and Xu et al. (2016).

At both high and low frequencies, the wind stress flux appears to have a strong positive coastal signal, notably on the western edge of the ocean basin at high frequencies and along the eastern edge at low frequencies. This signal arises primarily from the geostrophic velocity field and not the wind stress field and is therefore amplified in higher-resolution models. From our study of energy flux it is unclear what physical coastal process may lead to the flux of energy into motions across all frequencies along continental shelves.

The largest consistent signal in the wind stress flux at low frequencies across all models is located in the subtropics. Here there are alternating bands of positive and negative flux, with the largest amplitude in the Indian Ocean and weakening intensity to the east through the

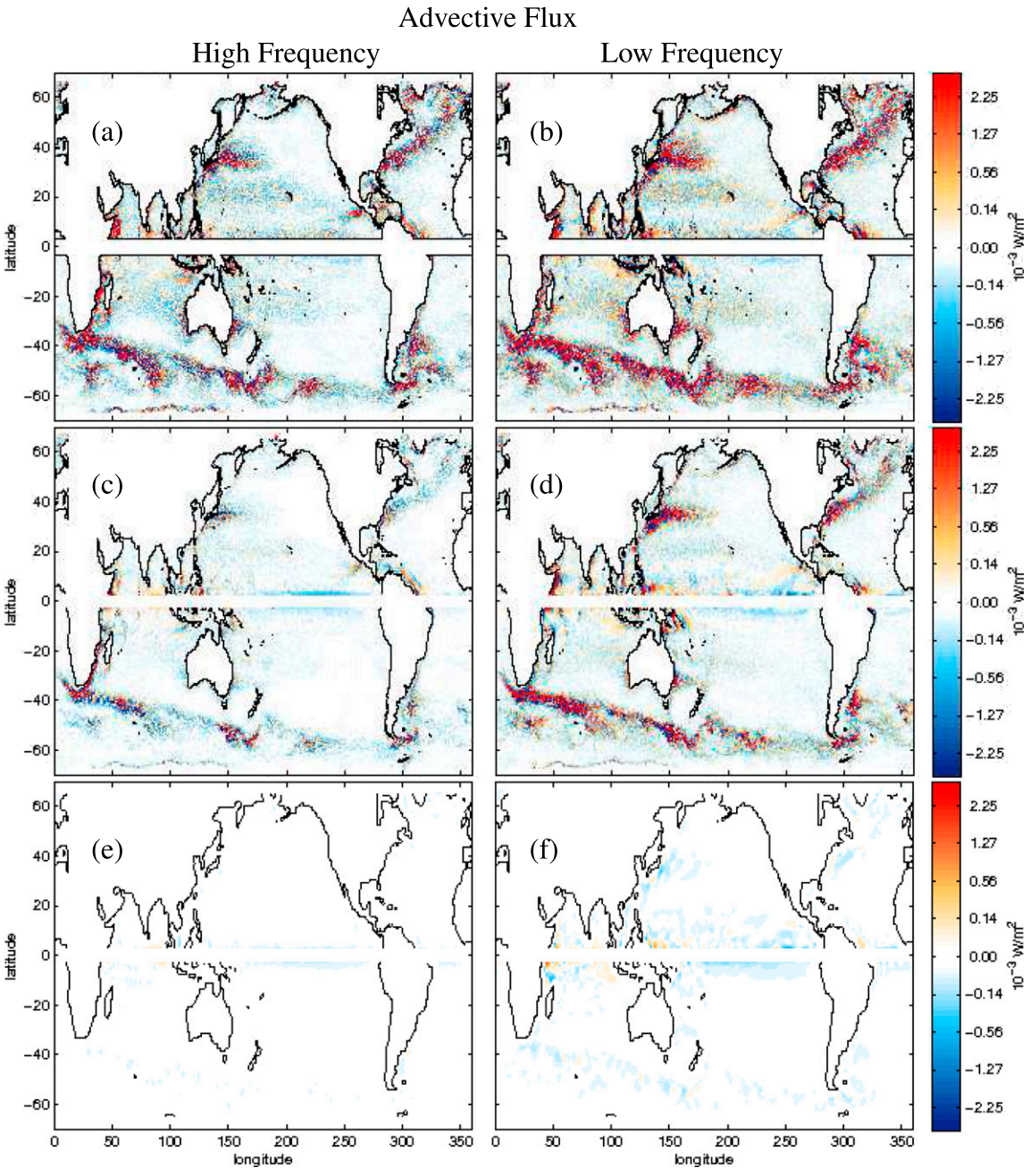

FIG. 9. Surface kinetic energy flux due to the advective term in (a),(b) CM2.6, (c),(d) CM2.5, and (e),(f) CM2–1d over (left) high and (right) low frequencies. High (low) frequencies are defined as motions with periods shorter (longer) than 3 months. Nonlinear color bars are employed in order to emphasize the sign of the low-amplitude signal.

Pacific and Atlantic. This pattern is potentially related to monsoonal and tropical atmospheric wave dynamics. The strong negative flux of energy out of eddying regions seen at high frequencies is again found at low frequencies.

In the global average the anomalous wind stress flux into the ocean is positive across high and low frequencies for all three models as seen in Table 1. The power input due to wind stress is comparable for high and low frequencies in CM2–1d as in CM2.5. However, the high-frequency wind stress flux in CM2.6, at 0.02 TW, is less than the CM2.6 wind stress flux at low frequency (0.04 TW). This difference is likely a result of increased ocean surface eddy resolution in CM2.6 and the negative wind stress flux associated with eddying regions at high frequencies in Fig. 10a. The sum of the

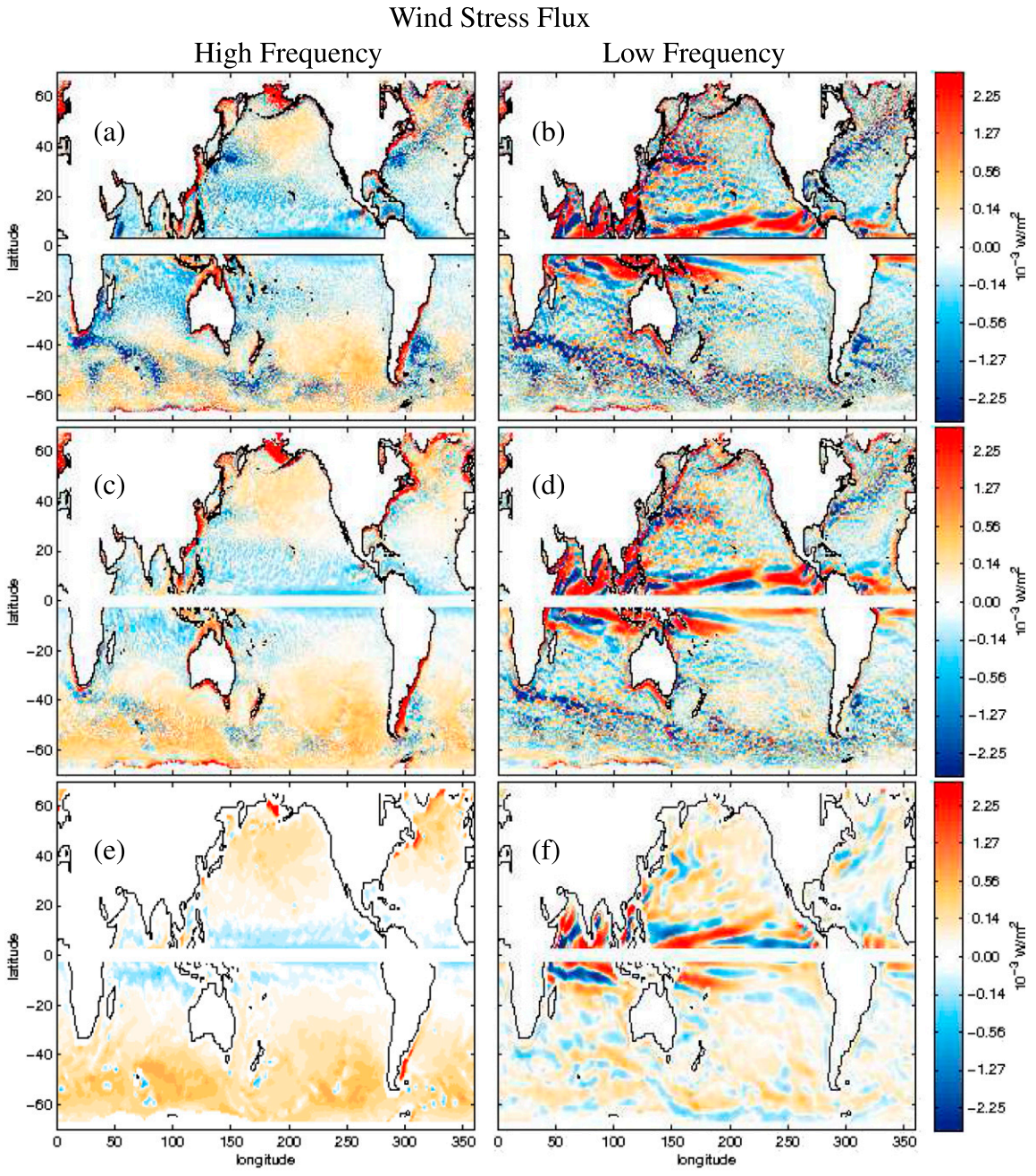

FIG. 10. Surface kinetic energy flux due to the wind stress term in (a),(b) CM2.6, (c),(d) CM2.5, and (e),(f) CM2–1d over (left) high and (right) low frequencies. High (low) frequencies are defined as motions with periods shorter (longer) than 3 months. Nonlinear color bars are employed in order to emphasize the sign of the low-amplitude signal.

wind stress flux over high and low frequencies in CM2.6 totals 0.06 TW and is less than the 0.07 TW calculated from Fig. 3. Following Eq. (4), these two values should be approximately equal. However, some energy is lost in the spectral flux calculation due to time windowing and the removal of the linear time trend within the data.

7. Conclusions and discussion

Low-frequency variability within the ocean surface must be maintained by either an energy flux to motions at long time scales or a direct forcing at low frequency. We consider here the transfer of kinetic energy across the frequency domain due to nonlinear horizontal

TABLE 1. Global averaged advective and wind stress fluxes over high and low frequencies for the three models in the CM2-O model hierarchy. Global advective and wind stress fluxes correspond to the maps in Figs. 9 and 10, respectively. Values are in TW.

	CM2–1d (TW)	CM2.5 (TW)	CM2.6 (TW)
Advection (high)	-5.25×10^{-5}	-5.63×10^{-3}	-7.35×10^{-3}
Advection (low)	-2.43×10^{-4}	6.51×10^{-3}	2.43×10^{-2}
Wind stress (high)	0.0321	0.0419	0.0185
Wind stress (low)	0.0317	0.0486	0.0382

advection and to atmospheric wind stress forcing in a hierarchy of three coupled climate models of varying ocean model horizontal resolution. There are additional sources of kinetic energy at long time scales, including the conversion of potential energy to kinetic energy, the effects of eddy viscosity, and vertical advection, that are not considered here due to the lack of subsurface information for all three models at the daily time scale. The full energy budget, including potential energy and heat within both the atmosphere and ocean, is beyond the scope of this research. In the three sections below, we summarize the conclusions drawn with respect to the three primary questions outlined in the introduction.

a. *The geostrophic inverse cascade*

Using the energy transfer Eq. (3) described by Hayashi (1980) and Arbic et al. (2012, 2014), we are able to observe the inverse cascade in wavenumber space within an open-ocean region in the South Pacific–Southern Ocean as shown in Figs. 5 and 6. Here we find that nonlinear advection transfers energy out of small spatial scales and adds energy to larger spatial scales. The inverse cascade in wavenumber space is observed in the eddying regions of both CM2.6 and CM2.5. However, the inverse cascade is not found in CM2–1d due to its limited horizontal resolution and lack of transient eddies.

Corresponding to the inverse cascade in wavenumber space, we find that energy is generally transferred from high frequencies to low frequencies due to the nonlinear advective term in the kinetic energy Eq. (3) as shown in global and regional averages in Fig. 7. The advective flux is spatially inhomogenous, as shown in Fig. 9, and attains its largest amplitude within eddying regions of the western boundary currents and the Southern Ocean. Notably, the pattern of negative and positive advective flux at high and low frequencies, respectively, is most evident in relatively quiescent regions away from strong currents as seen in Fig. 9. Within the narrow western boundary currents and the Southern Ocean eddying regions the advective flux term is of alternating sign at both high and low frequencies.

b. *Role of wind stress*

The wind stress transfer term as calculated in Eq. (3) is of comparable magnitude to the advective term in CM2.6 and CM2.5 as seen in the regional averages of Fig. 7, maps of the frequency-domain fluxes shown in Fig. 10, and global integrals given in Table 1. For these two models, the transfer of kinetic energy into a given frequency due to wind stress generally opposes that of the advective term. With the exception of the yearly time scale, the global and regional averages of Fig. 7 reveal that the wind stress generally acts to extract energy at low frequencies and add energy to high frequencies. The wind stress term transfers a significant amount of kinetic energy into the yearly time scale in the global average (Fig. 7a), the northwestern Pacific (Fig. 7b), and the eastern South Pacific (Fig. 7d). The synoptic-scale wind stress between days and weeks is the dominant source of energy within the South Atlantic sector of the Southern Ocean (Fig. 7c).

The spatial pattern of the wind stress flux displayed in Fig. 10 reveals that, at high frequencies, wind stress adds kinetic energy to the surface ocean mixed layer within the midlatitude storm tracks in either hemisphere and suppresses energy within the subtropical easterly wind bands. At low frequencies, the wind stress is of highest magnitude in the subtropics and Indian Ocean and is strongly negative within the eddying regions.

When averaged over regions, particularly eddying regions such as the northwestern Pacific and the South Atlantic–Southern Ocean area, wind stress removes energy at low frequencies and adds energy at high frequencies as seen in Fig. 7. It should be noted, however, that we are only considering the effect of the anomalous wind stress and ocean current fields in the calculation of $T_W(\omega)$ given in Eq. (3). We are not considering the large, dominant effect of the mean winds and the mean currents, which act as an energy source as shown in Fig. 3. The negative wind stress fluxes we observe here, particularly within the eddying regions, are a small correction to the overall positive flux of energy due to the time-mean wind stress acting on the time-mean oceanic general circulation. Nonetheless, these anomalous wind stress fluxes have a signature in the frequency domain that may impact or be signatures of embedded modes of low-frequency variability. The time-mean contribution, while larger than the anomalous contribution, has no time dependence by definition and is thus not indicative of the impact of temporal variability on the long-term climate.

The wind stress transfers are qualitatively similar across all three GFDL models, with the exception of a negative wind stress transfer at high frequencies within

the eddying regions of CM2.5 and CM2.6 (Fig. 10) that is absent in CM2–1d due to the lack of resolved eddies within this model. Given that the three coupled ocean models operate under atmospheric models with identical spatial resolutions, we infer that the changes in the wind stress term come primarily from changes within the geostrophic ocean surface velocities.

At 1° ocean model horizontal resolution atmospheric wind stress is stronger than advection across all frequencies in the global average (Fig. 7a). The higher-resolution models of CM2.6 and CM2.5 at 1/10° and 1/4° show a larger magnitude wind stress transfer than advective transfer. However, in CM2.6 and CM2.5 the advective transfer of kinetic energy out of high frequencies and into low frequencies, although smaller in overall magnitude than the wind stress term, acts to offset the effects of the anomalous wind power input. The kinetic energy budget across all time scales up to 20 years in CM2.6 and CM2.5 reveals a relative balance between wind stress and nonlinear advection, particularly in eddying regions where nonlinear advection is strong.

c. *Characteristic time scales and effects of model resolution*

Relative to CM2.6, CM2.5 displays slightly longer characteristic time scales for transfers in the frequency domain. Notably, the frequency at which transfers of wind stress and nonlinear advection change sign, or the transition frequency, is lower in CM2.5 than in CM2.6 as discussed in section 5c. The shift of the characteristic transfer signal in CM2.6 to lower frequency in CM2.5 may be related to slower geostrophic velocities in CM2.5 relative to CM2.6 following the Taylor hypothesis of Eq. (6).

To the extent that high-wavenumber ocean eddies have correspondingly high frequencies, we may expect that the geostrophic inverse cascade, or the transfer of energy from small spatial scales to large spatial scales, will carry over to frequency. Using the advective transfer diagnostic of Eq. (3) applied to CM2.5 and CM2.6, we have shown in Fig. 7 that energy does indeed tend to transfer from high to low frequencies in models with horizontal resolutions sufficient to support an oceanic eddy field. The advective term in the kinetic energy budget acts to extract energy out of high frequencies and supply energy to low frequencies, with a transition period between source and sink of approximately 3 months, in an analogous manner to the inverse cascade in wavenumber space.

Overall, CM2.6 has greater kinetic energy at low frequencies relative to the lower resolution models of CM2.5 and CM2–1d (Fig. 4), suggesting that the presence and representation of small-scale features within the ocean surface impacts low-frequency variability in coupled climate models. Through the advective transfer term, we have shown that surface geostrophic kinetic energy can be supplied from high frequencies to low frequencies due to nonlinear eddy–eddy interaction, which will be better represented with increasing horizontal resolution in the ocean model. The nonlinear advective transfer may then support the greater surface kinetic energy variance at low frequencies in higher-resolution models as seen in Fig. 4.

d. *Discussion*

Intrinsic low-frequency variability is of significant interest in understanding the behavior of the climate system at long time scales. We have found that the horizontal resolution of ocean models can influence the kinetic energy budget at long time scales and the characteristics of an inverse cascade due to intrinsic, nonlinear horizontal advection in frequency space. This work focuses solely on the contributions of nonlinear advection and wind stress to the frequency-domain kinetic energy budget. Further questions arise as to how these kinetic energy transfers balance those of potential-to-kinetic energy conversion, vertical advection, and eddy viscosity. However, the exploration of a full energy budget is beyond the scope of this research. Transfers within the full energy budget are more easily computed and interpreted in idealized studies that may provide insight into the physical processes behind the exchanges of energy in the frequency domain.

The CM2-O model hierarchy provides a foundation in which to determine the extent to which ocean model horizontal resolution impacts the exchange of energy between high and low frequencies. These models are fully coupled across the atmosphere and ocean such that changes in the ocean eddy field may impact larger-scale features of the climate as noted in Griffies et al. (2015). At the 0.5° horizontal resolution currently used in the atmospheric model, we find the wind stress field is similar across all three models. Increasing the atmospheric horizontal resolution may significantly and nonlinearly change the wind stress field within these models due to atmosphere–ocean coupling. Additionally, changes in or the addition of an eddy parameterization in the ocean may change the frequency response of the advective and wind stress transfer terms. A full sensitivity study of this nature is, however, beyond the scope of this current research.

The highest-resolution models in the CM2-O hierarchy, CM2.5 and CM2.6, do not include eddy parameterization. As described in Griffies et al. (2015), eddy parameterization schemes such as that of Gent and

McWilliams (1990) act to dissipate available potential energy and do not reinject energy directly into the kinetic energy budget that we focus on here. The CM2-O models do not include a backscatter parameterization scheme as in Jansen and Held (2014). As the backscatter parameterization scheme approximates the energetics of unresolved, subgrid-scale motions, it may have an impact on the transfer of kinetic energy at high frequencies.

In this paper we examine low-frequency variability in terms of the spectral energy budget at long time scales rather than diagnosing how these transfers relate to specific dynamical modes of variability such as the AMOC (Grégorio et al. 2015) or the variability of the Kuroshio Current Extension as described in Wang and Koblinsky (1995) and Qiu and Chen (2005). Nonetheless, this work shows that increasing horizontal resolution increases the magnitude of surface ocean kinetic energy transfers at time scales of relevance to major known modes of oceanic variability, such as at periods of months to decades. The relationship between resolution and kinetic energy transfer may further suggest a dynamical connection between small-scale eddies and known modes of low-frequency variability. Connecting intrinsic eddy dynamics to those of known, named modes of low-frequency variability is a topic of future work.

Acknowledgments. We would like to acknowledge the help and contribution of a number of individuals, including Mike Winton, Paul Spence, and Aidan Heerdegen. We also acknowledge the computing resources of NOAA GFDL and Princeton University. We would also like to thank three anonymous reviewers for their comments and time. This work is supported by NSF CAREER Grant OCE-1351837. The statements, findings, conclusions, and recommendations are solely the opinions of the authors and do not constitute a statement of policy, decision, or position on behalf of NOAA or the U.S. Government.

REFERENCES

Arbic, B. K., R. B. Scott, G. R. Flierl, A. J. Morten, J. G. Richman, and J. F. Shriver, 2012: Nonlinear cascades of surface oceanic geostrophic kinetic energy in the frequency domain. *J. Phys. Oceanogr.*, **42**, 1577–1600, doi:10.1175/JPO-D-11-0151.1.

——, M. Müller, J. G. Richman, J. F. Shriver, A. J. Morten, R. B. Scott, G. Sérazin, and T. Penduff, 2014: Geostrophic turbulence in the frequency–wavenumber domain: Eddy-driven low-frequency variability. *J. Phys. Oceanogr.*, **44**, 2050–2069, doi:10.1175/JPO-D-13-054.1.

Barnett, T. D., D. W. Pierce, R. Saravanan, N. Schneider, D. Dommenget, and M. Latif, 1999: Origins of the midlatitude Pacific decadal variablity. *Geophys. Res. Lett.*, **26**, 1453–1456, doi:10.1029/1999GL900278.

Charney, J., 1971: Geostrophic turbulence. *J. Atmos. Sci.*, **28**, 1087–1095, doi:10.1175/1520-0469(1971)028<1087:GT>2.0.CO;2.

Chelton, D. B., R. A. deSzoeke, M. G. Schlax, K. El Naggar, and N. Siwertz, 1998: Geographical variability of the first baroclinic Rossby radius of deformation. *J. Phys. Oceanogr.*, **28**, 433–460, doi:10.1175/1520-0485(1998)028<0433:GVOTFB>2.0.CO;2.

Delworth, T. L., and Coauthors, 2012: Simulated climate and climate change in the GFDL CM2.5 high-resolution coupled climate model. *J. Climate*, **25**, 2755–2781, doi:10.1175/JCLI-D-11-00316.1.

Duhaut, T. H. A., and D. N. Straub, 2006: Wind stress dependence on ocean surface velocity: Implications for mechanical energy input to ocean circulation. *J. Phys. Oceanogr.*, **36**, 202–211, doi:10.1175/JPO2842.1.

Dunne, J. P., and Coauthors, 2012: GFDLs ESM2 global coupled climate–carbon Earth system models. Part I: Physical formulation and the baseline simulation characteristics. *J. Climate*, **25**, 6646–6665, doi:10.1175/JCLI-D-11-00560.1.

Emery, W., and R. Thomson, 2014: *Data Analysis Methods in Physical Oceanography.* 3rd ed. Elsevier, 728 pp.

Farneti, R., T. L. Delworth, A. Rosati, S. Griffies, and F. Zeng, 2010: The role of mesoscale eddies in the rectification of the Southern Ocean response to climate change. *J. Phys. Oceanogr.*, **40**, 1539–1557, doi:10.1175/2010JPO4353.1.

Gent, P. R., and J. C. McWilliams, 1990: Isopycnal mixing in ocean general circulation models. *J. Phys. Oceanogr.*, **20**, 150–155, doi:10.1175/1520-0485(1990)020<0150:IMIOCM>2.0.CO;2.

Grégorio, S., T. Penduff, G. Sérazin, J.-M. Molines, B. Barnier, and J. Hirschi, 2015: Intrinsic variability of the Atlantic meridional overturning circulation at interannual-to-multidecadal timescales. *J. Phys. Oceanogr.*, **45**, 1929–1946, doi:10.1175/JPO-D-14-0163.1.

Gregory, J. M., and R. Tailleux, 2011: Kinetic energy analysis of the response of the Atlantic meridional overturning circulation to CO_2-forced climate change. *Climate Dyn.*, **37**, 893–914, doi:10.1007/s00382-010-0847-6.

Griffies, S. M., and Coauthors, 2015: Impacts on ocean heat from transient mesoscale eddies in a hierarchy of climate models. *J. Climate*, **28**, 952–977, doi:10.1175/JCLI-D-14-00353.1.

Hayashi, Y., 1980: Estimation of nonlinear energy transfer spectra by the cross-spectral method. *J. Atmos. Sci.*, **37**, 299–307, doi:10.1175/1520-0469(1980)037<0299:EONETS>2.0.CO;2.

Hirose, N., I. Fukumori, V. Zlotnicki, and R. M. Ponte, 2001: Modeling of the high-frequency barotropic response of the ocean to atmospheric disturbances: Sensitivity to forcing, topography, and friction. *J. Geophys. Res.*, **106**, 30 987–30 995, doi:10.1029/2000JC000763.

Hogg, A. McC., W. K. Dewar, P. D. Killworth, and J. R. Blundell, 2003: A quasi-geostrophic coupled model (Q-GCM). *Mon. Wea. Rev.*, **131**, 2261–2278, doi:10.1175/1520-0493(2003)131<2261:AQCMQ>2.0.CO;2.

Hoskins, B. J., and K. I. Hodges, 2005: A new perspective on Southern Hemisphere storm tracks. *J. Climate*, **18**, 4108–4129, doi:10.1175/JCLI3570.1.

Hua, B. L., and D. B. Haidvogel, 1986: Numerical simulations of the vertical structure of quasi-geostrophic turbulence. *J. Atmos. Sci.*, **43**, 2923–2936, doi:10.1175/1520-0469(1986)043<2923:NSOTVS>2.0.CO;2.

Jansen, M. F., and I. M. Held, 2014: Parameterizing subgrid-scale eddy effects using energetically consistent backscatter. *Ocean Modell.*, **80**, 36–48, doi:10.1016/j.ocemod.2014.06.002.

Jayne, S. R., and R. Tokmakian, 1997: Forcing and sampling of ocean general circulation models: Impact of high-frequency

motions. *J. Phys. Oceanogr.*, **27**, 1173–1179, doi:10.1175/1520-0485(1997)027,1173:FASOOG.2.0.CO;2.

Kirtman, B. P., and Coauthors, 2012: Impact of ocean model resolution on CCSM climate simulations. *Climate Dyn.*, **39**, 1303–1328, doi:10.1007/s00382-012-1500-3.

LaCasce, J. H., 1996: Baroclinic vorticies over a sloping bottom. Ph.D. thesis, Massachusetts Institute of Technology–Woods Hole Oceanographic Institution Joint Program in Physical Oceanography, 220 pp.

Larichev, V. D., and I. M. Held, 1995: Eddy amplitudes and fluxes in a homogenous model of fully developed baroclinic instability. *J. Phys. Oceanogr.*, **25**, 2285–2297, doi:10.1175/1520-0485(1995)025<2285:EAAFIA>2.0.CO;2.

Maltrud, M. E., and J. L. McClean, 2005: An eddy resolving global 1/10° ocean simulation. *Ocean Modell.*, **8**, 31–54, doi:10.1016/j.ocemod.2003.12.001.

Morten, A. J., 2015: Spatio-temporal spectra and spectral transfers in fluid dynamics. Ph.D. thesis, University of Michigan, 146 pp., doi:2027.42/116695.

Penduff, T., M. Juza, L. Brodeau, G. C. Smith, B. Barnier, J.-M. Molines, A.-M. Treguier, and G. Madec, 2010: Impact of global ocean model resolution on sea-level variability with emphasis on interannual time scales. *Ocean Sci.*, **6**, 269–284, doi:10.5194/os-6-269-2010.

——, ——, B. Barnier, J. Zika, W. K. Dewar, A.-M. Treguier, J.-M. Molines, and N. Audiffren, 2011: Sea level expression of intrinsic and forced ocean variabilities at interannual time scales. *J. Climate*, **24**, 5652–5670, doi:10.1175/JCLI-D-11-00077.1.

Qiu, B., and S. Chen, 2005: Variability of the Kuroshio Extension jet, recirculation gyre, and mesoscale eddies on decadal time scales. *J. Phys. Oceanogr.*, **35**, 2090–2103, doi:10.1175/JPO2807.1.

Rhines, P. B., 1979: Geostrophic turbulence. *Annu. Rev. Fluid Mech.*, **11**, 401–441, doi:10.1146/annurev.fl.11.010179.002153.

Roberts, M. J., and Coauthors, 2004: Impact of an eddy-permitting ocean resolution on control and climate change simulations with a global coupled GCM. *J. Climate*, **17**, 3–20, doi:10.1175/1520-0442(2004)017<0003:IOAEOR>2.0.CO;2.

——, H. T. Hewitt, P. Hyder, D. Ferreira, S. A. Josey, M. Mizielinski, and A. Shelly, 2016: Impact of ocean resolution on coupled air-sea fluxes and large-scale climate. *Geophys. Res. Lett.*, **43**, 10 430–10 438, doi:10.1002/2016GL070559.

Salmon, R., 1978: Two-layer quasi-geostrophic turbulence in a simple special case. *Geophys. Astrophys. Fluid Dyn.*, **10**, 25–52, doi:10.1080/03091927808242628.

——, 1980: Baroclinic instability and geostrophic turbulence. *Geophys. Astrophys. Fluid Dyn.*, **15**, 167–211, doi:10.1080/03091928008241178.

Saltzman, B., 1957: Equations governing the energetics of the larger scales of atmospheric turbulence in the domain of wave number. *J. Meteor.*, **14**, 513–523, doi:10.1175/1520-0469(1957)014<0513:EGTEOT>2.0.CO;2.

Scott, R. B., and F. Wang, 2005: Direct evidence of an oceanic inverse kinetic energy cascade from satellite altimetry. *J. Phys. Oceanogr.*, **35**, 1650–1666, doi:10.1175/JPO2771.1.

Small, R. J., and Coauthors, 2014: A new synoptic scale resolving global climate simulation using the Community Earth System Model. *J. Adv. Model. Earth Syst.*, **6**, 1065–1094, doi:10.1002/2014MS000363.

Steinberg, H. L., A. Winn-Nielsen, and C.-H. Yang, 1971: On nonlinear cascades in large-scale atmospheric flow. *J. Geophys. Res.*, **76**, 8629–8640, doi:10.1029/JC076i036p08629.

Stull, R. B., 2009: *An Introduction to Boundary Layer Meteorology.* Springer, 670 pp.

Taylor, G. I., 1938: The spectrum of turbulence. *Proc. Roy. Soc.*, **164**, 476–490, doi:10.1098/rspa.1938.0032.

Thorpe, S. A., 2007: *An Introduction to Ocean Turbulence.* Cambridge University Press, 266 pp.

Vallis, G., 2006: *Atmospheric and Oceanic Fluid Dynamics: Fundamentals and Large-scale Circulation.* Cambridge University Press, 770 pp.

von Storch, J.-S., H. Sasaki, and J. Marotzke, 2007: Wind-generated power input to the deep ocean: An estimate using a 1/10°general circulation model. *J. Phys. Oceanogr.*, **37**, 657–672, doi:10.1175/JPO3001.1.

——, H. Haak, E. Hertwig, and I. Fast, 2016: Vertical heat and salt fluxes due to resolved and parameterised meso-scale eddies. *Ocean Modell.*, **108**, 1–19, doi:10.1016/j.ocemod.2016.10.001.

Wang, L., and C. Koblinsky, 1995: Low-frequency variability in the regions of the Kuroshio Extension and the Gulf Stream. *J. Geophys. Res.*, **100**, 18 313–18 331, doi:10.1029/95JC01832.

Wunsch, C., 1998: The work done by the wind on the oceanic general circulation. *J. Phys. Oceanogr.*, **28**, 2332–2340, doi:10.1175/1520-0485(1998)028<2332:TWDBTW>2.0.CO;2.

Xu, C., X. Zhai, and X.-D. Shang, 2016: Work done by atmospheric winds on mesoscale ocean eddies. *Geophys. Res. Lett.*, **43**, 12 174–12 180, doi:10.1002/2016GL071275.

Zhai, X., H. L. Johnson, D. P. Marshall, and C. Wunsch, 2012: On the wind power input to the ocean general circulation. *J. Phys. Oceanogr.*, **42**, 1357–1365, doi:10.1175/JPO-D-12-09.1.